

# Efficient Ptychography Reconstruction using the Hessian operator

MARCUS CARLSSON,<sup>1,\*</sup> VIKTOR NIKITIN,<sup>2</sup> HERWIG WENDT<sup>3</sup>

<sup>1</sup> Centre for Mathematical Sciences, Lund University, Sölvegatan 18, 223 62 Lund, Sweden

<sup>2</sup> Advanced Photon Source, Argonne National Laboratory, 9700 S Cass Ave, Lemont, IL 60439, USA

<sup>3</sup> IRIT Laboratory, University of Toulouse, 2 rue Camichel, 31000 Toulouse, France

\*marcus.carlsson@math.lu.se

**Abstract:** Ptychography reconstruction is typically performed using first-order methods, such as gradient descent, due to their computational efficiency. Higher-order methods, while potentially more accurate, are often prohibitively expensive in terms of computation. In this study, we present a mathematical formulation for reconstruction using second-order information, derived from an efficient computation of the bilinear Hessian and Hessian operator. The formulation is provided for both Gaussian and Poisson models, enabling the simultaneous reconstruction of the object, probe, and positions. Synthetic data tests, along with experimental near-field ptychography data processing, demonstrate a 10x performance improvement compared to first-order methods. The derived formulas for computing the Hessians, along with the strategies for incorporating them into optimization schemes, are well-structured and easily adaptable to various ptychography problem formulations.

## 1. Introduction

The increasing availability of coherent X-ray sources has significantly advanced the use of ptychography, a coherent diffraction imaging (CDI) technique that enables nano-resolution imaging without the need for traditional optical lenses. In ptychography, a focused beam, referred to as the "probe", illuminates the sample that is shifted laterally through different positions, and the resulting diffraction patterns are recorded by a detector. The image is then reconstructed using computational phase retrieval methods. Depending on the experimental configuration, ptychography can be classified into near-field and far-field variants.

Near-field ptychography for nano-resolution imaging is typically performed with the sample positioned at a specific distance from the focal spot [1, 2]. A schematic of the setup is shown in Figure 1,a. The distance defines geometrical magnification. The detector is placed about 1 to 1.5 meters from the focal spot, placing the system in the Fresnel regime. In this setup, diffraction patterns arise from the interference between the scattered and undiffracted beams, which are mathematically described by a Fresnel transform.

In contrast, far-field ptychography is employed when the sample is placed at or near the focal spot [3, 4], see Figure 1,b. The detector is positioned much farther away, typically around 3 meters. This configuration corresponds to the Fraunhofer regime, where the diffraction patterns formation is described by the Fourier transform. Due to the smaller sample illumination area in far-field ptychography, the number of scanning positions required is typically much higher compared to near-field ptychography. In far-field ptychography, the beam is typically focused with zone plates, whereas in near-field ptychography, Kirkpatrick-Baez (KB) mirrors are used.

Both near-field and far-field ptychography techniques have found significant applications across a range of disciplines, including materials science, biology, and nanotechnology, enabling three-dimensional imaging at resolutions that surpass traditional microscopy [5–8].

In typical ptychography experiments, reconstruction is performed for both the object  $\psi$  and the probe  $q$ . Additionally, scan positions refinement is necessary to correct for potential motor errors. Most modern ptychography algorithms rely on optimization of a objective functional  $f$ . While it is well known in optimization that knowledge of the second order derivatives of this functional,

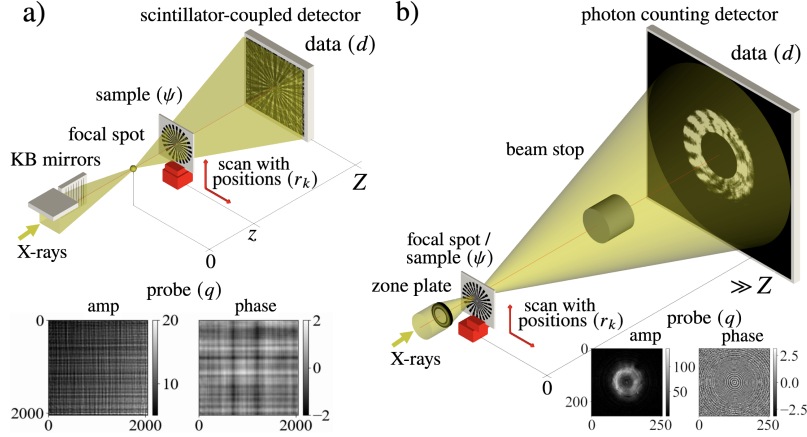


Fig. 1. Experimental setups for (a) near-field ptychography where the X-ray beam is focused using Kirkpatrick-Baez (KB) mirrors, and the diffraction patterns are captured in the Fresnel regime, and (b) far-field ptychography where the beam is focused by a zone plate, and diffraction patterns are recorded in the Fraunhofer regime. Both setups include examples of the recovered probe amplitude and phase distributions.

the so called ‘‘Hessian’’ matrix  $\nabla^2 f|_{\mathbf{x}}$  or  $\mathbf{H}^f|_{\mathbf{x}}$  (where  $\mathbf{x}$  is the point of evaluation), can be used to speed up convergence significantly, this is usually not used in ptychography. This is partially due to the fact that the Hessian matrix is considered to have a complicated structure [9], but primarily because the amount of variables in  $\psi$  that need to be reconstructed in a standard size modern application typically is of the order  $10^4 \times 10^4$ . Thus, upon arranging these variables in a vector, the Hessian matrix would be of the size  $10^8 \times 10^8$ , which is about 71 petabytes of complex numbers, each represented by two 32-bit floating point values. This clearly makes it prohibitively slow or impossible to handle, and therefore first order methods and various types of alternating projection schemes are predominant, see [10] for a recent survey. Even for smaller scale experiments where  $\psi$  is say  $10^3 \times 10^3$  and the probe is known, computing and storing the Hessian via standard calculus is not feasible, although it has been tried e.g. in [11] where the numerical section displays results for  $32 \times 32$ -images.

The goal of this work is to introduce a new approach for efficiently using exact second order information in ptychography reconstruction, able to scale to large problem sizes such as those cited above. To convey the key idea behind our method, assume for the moment that we have column-stacked our unknown variables so that they are represented by vectors  $\mathbf{x}$  in  $\mathbb{R}^n$  (where  $n$  is huge), and suppose that we make use of an iterative reconstruction algorithm (i.e., a descent algorithm) and arrived at point  $\mathbf{x}_k$ . If we knew the gradient  $\nabla f|_{\mathbf{x}_k}$  and the Hessian matrix  $\mathbf{H}^f|_{\mathbf{x}_k}$  of  $f$  at  $\mathbf{x}_k$ , we would have the following quadratic approximation

$$f(\mathbf{x}_k + \alpha \mathbf{s}_k) \approx f(\mathbf{x}_k) + \alpha \langle \nabla f|_{\mathbf{x}_k}, \mathbf{s}_k \rangle + \frac{\alpha^2}{2} \langle \mathbf{H}^f|_{\mathbf{x}_k} \mathbf{s}_k, \mathbf{s}_k \rangle \quad (1)$$

and could make use of it in several ways in the process of determining the next point  $\mathbf{x}_{k+1}$ :

1. An *optimal step size*  $\alpha_k$  known as Newton’s rule could be determined given a descent direction  $\mathbf{s}_k$  (e.g., the gradient  $\nabla f|_{\mathbf{x}_k}$ ) by setting  $\alpha_k = -\frac{\langle \nabla f|_{\mathbf{x}_k}, \mathbf{s}_k \rangle}{\langle \mathbf{H}^f|_{\mathbf{x}_k} \mathbf{s}_k, \mathbf{s}_k \rangle}$ .
2. The *conjugate gradient* (CG) method could be used with the principled conjugate directions known as Daniel’s rule [12] (instead of the many heuristic rules that have been proposed to

avoid computing the Hessian, see; e.g., the overview article [13] and the recent book [14]), which requires computing the real number  $\langle \mathbf{H}^f|_{\mathbf{x}_k} \mathbf{s}_k, \mathbf{t}_k \rangle$  for two vectors  $\mathbf{s}_k$  and  $\mathbf{t}_k$ .

3. *Newton descent direction*  $\mathbf{s}_k$  for second order (Quasi-)Newton algorithms could be obtained by (approximately) solving for  $\mathbf{s}_k$  the equation

$$-\nabla f|_{\mathbf{x}_k} = \mathbf{H}^f|_{\mathbf{x}_k} \mathbf{s}_k. \quad (2)$$

In order to make use of these concepts in large scale problems, following the general ideas outlined in our theoretical paper [15], the first key observation is that none of the above expressions requires knowledge of the Hessian *matrix*, but only computation of one real number  $\langle \mathbf{H}^f|_{\mathbf{x}} \mathbf{s}, \mathbf{t} \rangle$ , or one vector  $\mathbf{H}^f|_{\mathbf{x}} \mathbf{s}$  in the case of the matrix-vector multiplication (2). The second is that, once we have disposed of the matrix-vector multiplication, we can also dispose of the column-stacking (i.e. the vectors) and represent data and the unknown variables *in their natural domains*, i.e. 3D-tensors and matrices, which further enables efficient and transparent implementation of the relevant operators in the reconstruction algorithm. Our approach makes it possible to identify the *analytic expressions* for the above quantities  $\langle \mathbf{H}^f|_{\mathbf{x}} \mathbf{s}, \mathbf{t} \rangle$  and  $\mathbf{H}^f|_{\mathbf{x}} \mathbf{s}$  henceforth referred to as the *bilinear Hessian* and the *Hessian operator*, and to completely avoid the Wirtinger-type derivatives traditionally used for these type of computations. The mathematical framework we consider is fairly general and works for blind ptychography with uncertain scanning positions, both for far and near field ptychography and with either Gaussian or Poisson noise. Our focus here is on describing the mathematical tools, rather than using this information to design or promote any particular algorithm, since ptychography problems come in a number of different settings, all with specialized algorithms designed for the particular issues arising in the given experimental setup.

The remainder of this work is organized as follows. Section 2 introduces the mathematical framework for ptychography reconstruction. Section 3 briefly defines the bilinear Hessian and the Hessian operators as mathematical objects, and our proposed Gradient descent (GD), Conjugate Gradient (CG) and Quasi-Newton (QN) descent algorithms based on these operators; a detailed and general mathematical treatment thereof is given in [15]. Moreover, we proof as a key contribution the chain rule for bilinear Hessians, which allows us to decompose the computations into simple, transparent steps. In Section 4, we compute simplified expressions for the gradient, the bilinear Hessian and the Hessian operator for Gaussian noise and for Poisson noise. In Section 5, we compose these expressions with the operators acting in the full ptychography problem with probe retrieval using the chain rule for bilinear Hessians and obtain the expressions for the bilinear Hessian, and in Section 6 we derive the expressions for the Hessian operator. The derivation of the expressions for blind ptychography with uncertain shift positions is detailed in Section 7. In Section 8, we report results for numerical experiments for simulated as well as experimental near-field ptychography data acquired at beamline ID16A of the European Synchrotron Radiation Facility (ESRF) and show that our proposed approach compares very favorably to the state of the art in terms of computational cost and accuracy. Section 9 concludes on this work and points to future research.

## 2. Mathematical framework for ptychography

We are interested in reconstructing an unknown “object”  $\psi$  (or rather, the complex wave-field right behind the object), which mathematically is represented as a matrix in  $\mathbb{C}^{N \times N}$ . For each scanning position  $r_k = (x_k, y_k) \in \mathbb{R}^2$ , where  $k = 1, \dots, K$ , a submatrix in  $\mathbb{C}^{M \times M}$ , which we denote by  $\psi_{r_k}$ , gets illuminated by a “probe”  $q$  (also represented as a complex matrix  $\mathbb{C}^{M \times M}$ ), and the joint wave-field  $q \cdot \psi_{r_k}$  gets propagated to the detector by a diffraction operator  $D$ , such as the Fresnel transform (for near-field ptychography) or the Fourier transform (for far-field ptychography). Here  $\cdot$  denotes elementwise multiplication of the matrices (a.k.a. Hadamard

multiplication). On the detector, only the intensity of the incoming field is measurable, i.e., for a given scanning position, each pixel value  $(m_1, m_2)$  on the detector measures

$$i_{m_1, m_2, k} = |(D(q \cdot \psi_{r_k}))_{m_1, m_2}|^2.$$

Thus data naturally comes arranged as a 3D-tensor  $\mathbb{R}^{M \times M \times K}$ , and the ptychography problem consists in retrieving the full matrix  $\psi$ , along with the probe  $q$ , from these measurements. The amplitude-based model provides more robust solutions than the intensity-based model, as concluded in [11, 16], so henceforth our “data” will be  $d_{m_1, m_2, k} = \sqrt{i_{m_1, m_2, k}}$ .

In summary, we wish to retrieve  $(q, \psi) \in \mathbb{C}^{M \times M} \times \mathbb{C}^{N \times N}$  given data  $d \in \mathbb{R}^{M \times M \times K}$ . Eventually we will also consider the scanning positions as unknowns, but for the moment we ignore this for clarity of the exposition. The forward model, in the absence of noise, can be written as

$$d = |D_K(I_K(q) \cdot S_r(\psi))| \quad (3)$$

where

- $S_r$  is the operator which, for each scanning position  $r_k$ , “extracts” the illuminated part  $\psi_{r_k}$  of  $\psi$  and arranges these “slices” in a  $\mathbb{C}^{M \times M \times K}$ -tensor
- $I_K(q)$  denotes  $K$  copies of  $q$  arranged in the same  $\mathbb{C}^{M \times M \times K}$ -tensor
- $\cdot$  denotes element-wise multiplication of tensors
- $D_K$  is the operator on  $\mathbb{C}^{M \times M \times K}$  that takes each  $\mathbb{C}^{M \times M}$ -slice of the tensor and propagates it to the detector via  $D$ .

Note that  $S_r$ ,  $I_K$  and  $D_K$  are linear operators acting on the argument following. When implementing in, e.g., Python, the operators  $I_K$  and  $D_K$  do not need to be considered explicitly since Python automatically distributes over the third variable when 3D tensors and matrices with compatible dimensions are multiplied, suggesting that they are also superfluous in the mathematical framework. However, they are needed because the computation of the adjoint operators is also required, which involves summing operators over the third variable and needs to be coded explicitly.

In addition to (3), one needs to take into account noise. The noise is assumed to be Gaussian if there is a high photon-count on the detector (typically near-field ptychography), and it is typically assumed to be Poisson in the opposite scenario (e.g., far-field ptychography), although the noise is often approximated as Gaussian also in the latter case to accelerate convergence [16, 17]. As explained in e.g. [16], one wishes to minimize the negative log-likelihood of the joint probability distribution, which in the case of Gaussian noise leads to the problem of finding the global minima of the following objective functional

$$f^G(q, \psi) = \sum_{\gamma \in \Gamma} w_\gamma \left( |D_K(I_K(q) \cdot S_r(\psi))_\gamma| - d_\gamma \right)^2, \quad (4)$$

where  $\Gamma$  denotes the index set  $\{1, \dots, N\}^2 \times \{1, \dots, K\}$  and  $w_\gamma$  is a weight which is zero at positions of the beamstop and other possibly faulty detector positions. In particular, note that the weight usually will not depend on the third variable (since the detector/beamstop are the same between different measurements), but it is notationally simpler to let  $w$  depend on all variables in  $\Gamma$ . In the case of Poisson noise, the corresponding functional reads

$$f^P(q, \psi) = \sum_{\gamma \in \Gamma} w_\gamma \left( \left| D_K(I_K(q) \cdot S_r(\psi))_\gamma \right|^2 - 2d_\gamma \log \left( |D_K(I_K(q) \cdot S_r(\psi))_\gamma| \right) \right). \quad (5)$$

### 3. A general vectorization-free optimization framework

The functionals introduced in the previous section act on the linear space  $\mathbb{X} := \mathbb{C}^{M \times M} \times \mathbb{C}^{N \times N}$ . On the other hand, most optimization methods are developed for  $\mathbb{R}^n$ , which is perfectly applicable in this setting since, upon ordering the elements and considering real and imaginary parts separately, we can identify  $\mathbb{X}$  with  $\mathbb{R}^n$  where  $n = 2M^2 + 2N^2$ . This operation is usually done by column-stacking the matrices and then concatenating the resulting vectors. We will use the convention that any element  $x \in \mathbb{X}$ , when represented as a vector, is denoted in bold by  $\mathbf{x}$ , and vice versa.

Thus, let us denote two arbitrary elements of the former space by  $x$  and  $y$  and their respective representations in  $\mathbb{R}^n$  by  $\mathbf{x}$  and  $\mathbf{y}$ . The *bilinear Hessian*  $\mathcal{H}^f|_x$  of a given functional  $f$ , evaluated at a given point  $x \in \mathbb{X}$ , is the unique symmetric bilinear form on  $\mathbb{X}$  such that we always have

$$\mathcal{H}^f|_x(u, v) = \langle \mathbf{H}^f|_x \mathbf{u}, \mathbf{v} \rangle,$$

where  $\mathbf{H}^f$  is the Hessian matrix of  $f$  when considered as a functional acting on  $\mathbb{R}^n$  in the obvious way. In [15], we introduced a general technique for efficiently computing bilinear Hessians in large scale optimization settings such as the present. The core of our approach relies on Taylor expansions and Fréchet-style derivatives in inner product spaces, which allows us to avoid using column-stacking operation, the classical chain rule and Wirtinger derivatives. Given the expressions for  $f := f^G$  or  $f^P$  from (4) or (5), we can derive expressions for  $\mathcal{H}^f|_x$  that do not rely on second order derivatives of  $f$  (explicitly at least) and moreover are efficiently implementable. Along the same lines, we introduced an efficiently computable forward operator  $H^f|_x$  acting on  $\mathbb{X}$ , termed the *Hessian operator*, with the property that  $H^f_x(u) = v$  holds if and only if  $\mathbf{v} = \mathbf{H}^f_x \mathbf{u}$  holds. The mathematical details are explained in greater detail in the next section.

#### 3.1. Differential calculus in linear spaces

In this section we briefly recapitulate the the main points of [15] and also introduce a sort of chain rule for computation of the bilinear Hessian. The key idea is to introduce a framework in which one can work with the gradient and Hessian in general linear spaces, without having to introduce a basis and resort to multivariable calculus.

Given two real inner product spaces  $\mathbb{X}$  and  $\mathbb{Y}$  and a function  $\mathcal{L} : \mathbb{X} \rightarrow \mathbb{Y}$ , we define the Fréchet derivative of  $\mathcal{L}$  at some  $x_0 \in \mathbb{X}$  as the (unique) linear operator  $d\mathcal{L}|_{x_0}$  such that

$$\mathcal{L}(x_0 + \Delta x) = \mathcal{L}(x_0) + d\mathcal{L}|_{x_0}(\Delta x) + \mathcal{O}(\|\Delta x\|^2),$$

of course, assuming that such exists. Here and elsewhere,  $\Delta x$  denotes an independent “small” variable in  $\mathbb{X}$ . Similarly, we define the second order derivative as the (unique) bilinear symmetric  $\mathbb{Y}$ -valued operator such that

$$\mathcal{L}(x_0 + \Delta x) = \mathcal{L}(x_0) + d\mathcal{L}|_{x_0}(\Delta x) + \frac{1}{2}d^2\mathcal{L}|_{x_0}(\Delta x, \Delta x) + \mathcal{O}(\|\Delta x\|^3). \quad (6)$$

Of course, if  $\mathbb{X} = \mathbb{R}^n$  and  $\mathbb{Y} = \mathbb{R}$ , then the latter is simply the Hessian and the former becomes a linear functional and can be rewritten

$$d\mathcal{L}|_{x_0}(\Delta x) = \langle \nabla \mathcal{L}|_{x_0}, \Delta x \rangle,$$

where for some element  $\nabla \mathcal{L}|_{x_0} \in \mathbb{X}$  that denotes the gradient. In this paper, the space  $\mathbb{X}$  is typically a space of complex matrices or 3D-tensors. These spaces are naturally endowed with the complex inner product

$$\langle X, Y \rangle = \sum_{\gamma \in \Gamma} X_\gamma \overline{Y_\gamma},$$

where  $\Gamma$  denotes the index set, i.e.  $\{1, \dots, L\} \times \{1, \dots, M\}$  for  $L \times M$ -matrices and  $\{1, \dots, L\} \times \{1, \dots, M\} \times \{1, \dots, N\}$  for  $L \times M \times N$ -tensors. However, in the proposed formulation, we can view these spaces as linear spaces over  $\mathbb{R}$ , where the new scalar product is given by

$$\langle X, Y \rangle_{\mathbb{R}} = \text{Re}\langle X, Y \rangle, \quad (7)$$

and then the machinery developed in this section applies all the same. Note in particular that the formula (6) does not rely on whether the scalar product is real or imaginary, so regardless the objects  $d\mathcal{L}$  and  $d^2\mathcal{L}$  are the same, and typically take complex numbers if  $\mathbb{Y}$  is also a complex space. However, if  $\mathbb{Y}$  equals  $\mathbb{R}$  then of course the values of  $d\mathcal{L}$  are real and, in order to use this to obtain a *gradient*, it is crucial to use the real scalar product. In this case, we will typically denote  $\mathcal{L}$  by  $f$  and we define the gradient of  $f$ , denoted  $\nabla f|_{x_0}$ , as the unique element in  $\mathbb{X}$  such that

$$Df|_{x_0}(\Delta x) = \langle \nabla f|_{x_0}, \Delta x \rangle. \quad (8)$$

Moreover  $d^2\mathcal{L}$  is then called the bilinear Hessian which we denote by  $\mathcal{H}^f$ , and we define the *Hessian operator* as the unique symmetric real linear operator  $H^f : \mathbb{X} \rightarrow \mathbb{X}$  such that

$$\mathcal{H}^f(\Delta y, \Delta z) = \langle H^f(\Delta y), \Delta z \rangle_{\mathbb{R}} \quad (9)$$

holds for all  $\Delta y, \Delta z \in \mathbb{X}$ . Armed with these definitions, we can now generalize (1) to a completely vector free setting as follows

$$f(x_0 + y) \approx f(x_0) + \langle \nabla f|_{x_0}, y \rangle + \frac{1}{2} \mathcal{H}^f|_{x_0}(y, y) \quad (10)$$

Again, we refer to [15] for a fuller discussion of these concepts. Expressions for  $\nabla f|_{x_0}$  and  $\mathcal{H}^f|_{x_0}$  for the concrete functionals at hand (i.e. (4) and (5)) are derived in Sections 4 and 5, and the Hessian operator is derived in Section 6. The problem with position correction is studied in Section 7.

The proposed approach bears equivalences with the use Wirtinger derivatives in the sense that it generalizes the notion of gradients to functions on complex spaces. However, the proposed method relies on Fréchet derivatives to generalize this to multidimensional objects, which are more versatile than the standard derivatives used in Wirtinger calculus. This allows for the handling of more complicated functionals that are difficult to express using Wirtinger derivatives. Moreover, by deriving gradients through Taylor expansions rather than manipulating Wirtinger derivatives, the proposed approach offers simpler and more intuitive expressions. This generalization not only retains the familiar computational structure but also provides greater flexibility, making it particularly powerful for advanced applications in Ptychography.

### 3.2. The chain rule for bilinear Hessians

In order to keep the corresponding expressions as simple as possible and facilitate easy implementation, it is crucial to write the full objective functional as a composition of simpler functionals and then rely on a *chain rule* for bilinear Hessians. Specifically, we now consider how to efficiently compute the above objects for composite functions  $\mathcal{J} = \mathcal{K} \circ \mathcal{L}$ , where  $\mathcal{K} : \mathbb{Y} \rightarrow \mathbb{Z}$  is another function between inner product spaces. We then have

**Theorem 1** *Let  $x_0 \in \mathbb{X}$  be given and set  $y_0 = \mathcal{L}(x_0)$ . The joint derivative of  $\mathcal{J}$  at  $x_0$  is then given by*

$$d\mathcal{J}|_{x_0}(v) = d\mathcal{K}|_{y_0}(d\mathcal{L}|_{x_0}(v)), \quad v \in \mathbb{X}. \quad (11)$$

*Moreover, the second order derivative is given by*

$$d^2\mathcal{J}|_{x_0}(v, w) = d^2\mathcal{K}|_{y_0}(d\mathcal{L}|_{x_0}(v), d\mathcal{L}|_{x_0}(w)) + d\mathcal{K}|_{y_0}(d^2\mathcal{L}|_{x_0}(v, w)). \quad (12)$$

We remark that, in the case  $\mathbb{Z} = \mathbb{R}$  and, denoting  $\mathcal{J}$  by  $f$ , the formula (11) can be recast as

$$\nabla f|_{x_0} = d\mathcal{L}|_{x_0}^*(\nabla f|_{y_0}), \quad (13)$$

where  $\cdot^*$  denotes the operator adjoint. Note that this formula holds also if  $\mathbb{X}$  and  $\mathbb{Y}$  are complex spaces due to (7).

*Proof:* Set  $\Delta y = \mathcal{L}(x_0 + \Delta x) - \mathcal{L}(x_0)$ . We then have

$$\Delta y = d\mathcal{L}|_{x_0}(\Delta x) + \frac{1}{2}d^2\mathcal{L}|_{x_0}(\Delta x, \Delta x) + O(\|\Delta x\|^3).$$

By (6) applied to  $\mathcal{K}$  at  $y_0$  we thus get

$$\begin{aligned} \mathcal{K}(\mathcal{L}(x_0 + \Delta x)) &= \mathcal{K}(y_0) + d\mathcal{K}|_{y_0}(\Delta y) + \frac{1}{2}d^2\mathcal{K}|_{y_0}(\Delta y, \Delta y) + O(\|\Delta y\|^3) = \\ &= \mathcal{K}(\mathcal{L}(x_0)) + d\mathcal{K}|_{y_0}\left(d\mathcal{L}|_{x_0}(\Delta x) + \frac{1}{2}d^2\mathcal{L}|_{x_0}(\Delta x, \Delta x)\right) + \\ &+ \frac{1}{2}d^2\mathcal{K}|_{y_0}\left(d\mathcal{L}|_{x_0}(\Delta x), d\mathcal{L}|_{x_0}(\Delta x)\right) + O(\|\Delta x\|^3). \end{aligned}$$

By the linearity of  $d\mathcal{K}|_{y_0}$  and the uniqueness of the operators in (6) (which is proved in [15]), the formula (11) is immediate as well as the identity

$$d^2\mathcal{J}|_{x_0}(\Delta x, \Delta x) = d^2\mathcal{K}|_{y_0}(d\mathcal{L}|_{x_0}(\Delta x), d\mathcal{L}|_{x_0}(\Delta x)) + d\mathcal{K}|_{y_0}(d^2\mathcal{L}|_{x_0}(\Delta x, \Delta x)).$$

Similarly, (12) follows by uniqueness of symmetric bilinear operators in expressions such as (6), since indeed (12) is a bilinear symmetric operator which agrees with the above expression on the diagonal  $v = w = \Delta x$ .  $\square$

### Manual computation versus Automatic Differentiation

Depending on the way the problem is tackled, deriving the sought gradients and operators can lead to long and complicated expression and their implementation can become a challenge, an obstacle which has led various authors to argue in favor of the use of Automatic Differentiation (AD) [18, 19]. However, as has been noted e.g. in [20], this is often substantially slower than using analytical expressions derived manually (see Section 3.3 of [15] for a more detailed discussion, and where the computation of the Hessian operator is shown to be up to one order of magnitude slower with AD already for a very simple example). We will demonstrate the same conclusion for the problem at hand in Section 8. Moreover, as noted in Section 4.5 of [21], Automatic Differentiation works poorly in combination with certain modifications, such as preconditioning (which is crucial for the problem at hand), and therefore it is hard to avoid laborious manual computations either way (see Appendix B of [21]). The proposed framework for deriving the sought gradients and operators is mechanical, and although the length of the so-obtained expressions also reflects the complexity of the problem to some extent, our expressions are transparent and easy to implement and test, thanks to derivative-free computations and the use of the chain rule for the bilinear Hessian. We therefore argue that manual computation, relying on the proposed framework, is preferable to AD.

### 3.3. Optimization algorithms

Before moving on to the concrete expressions that form the core of our contribution, let us briefly discuss how these can be used in various standard optimization methods such as Gradient Descent, Conjugate Gradient and Quasi-Newton algorithms with Newton step size for ptychography reconstruction. We term these algorithms BH-GD, BH-CG and BH-QN, respectively, where ‘‘BH’’ stands for ‘‘bilinear Hessian’’.

### 3.3.1. Gradient descent and Newton step size

Given a direction  $s_k$ , a near optimal strategy for step length for the step  $x_{k+1} = x_k + \alpha_k s_k$  is to set  $x_0 = x_k$  and  $y = \alpha s_k$  in the right hand side of (10) and minimize with respect to  $\alpha$ , which yields

$$\alpha_k = -\frac{\langle \nabla f|_{x_k}, \mathbf{s}_k \rangle}{\mathcal{H}^f|_{x_k}(s_k, s_k)}. \quad (14)$$

In particular, if  $s_k = -\nabla f|_{x_k}$ , this gives the Gradient Descent method with Newton step-size;

$$x_{k+1} = x_k - \frac{\|\nabla f|_{x_k}\|^2}{\mathcal{H}^f|_{x_k}(\nabla f|_{x_k}, \nabla f|_{x_k})} \nabla f|_{x_k}. \quad (15)$$

### 3.3.2. Conjugate Gradient method

The original CG method was developed as a fast solver to equations of the form  $\mathbf{H}\mathbf{x} = \mathbf{d}$ , where  $\mathbf{H}$  is a positive definite matrix on  $\mathbb{R}^n$  and  $\mathbf{d}$  represents some measured data [22]. It makes use of directions  $\mathbf{s}_k = -\nabla f|_{x_k} + \beta_k \mathbf{s}_{k-1}$ , where  $\beta_k$  is chosen so that  $\langle \mathbf{s}_k, \mathbf{H}\mathbf{s}_{k-1} \rangle = 0$ , leading to the formula  $\beta_k = \langle \nabla f|_{x_k}, \mathbf{H}\mathbf{s}_{k-1} \rangle / \langle \mathbf{s}_{k-1}, \mathbf{H}\mathbf{s}_{k-1} \rangle$ . For non-quadratic functionals, this expression for  $\beta_k$  can be rewritten in many ways, leading to competing heuristic formulas such as Fletcher-Reeves [23], Polak-Ribière [24], Hestenes-Stiefel [22], Dai-Yuan [25] and Hager-Zhang [26]. Direct transposition of of the expression for  $\beta_k$  to the non-quadratic setting leads to

$$\beta_k = \frac{\mathcal{H}^f|_{x_k}(\nabla f|_{x_k}, s_{k-1})}{\mathcal{H}^f|_{x_k}(s_{k-1}, s_{k-1})}, \quad (16)$$

which was proposed by Daniel [12] but is rarely used because the computation of the Hessian was considered as a deadlock. Our expressions for the bilinear Hessian lift this deadlock, and we can define the following CG method with Newton step size:

$$x_{k+1} = x_k - \frac{\langle \nabla f|_{x_k}, s_k \rangle}{\mathcal{H}^f|_{x_k}(s_k, s_k)} s_k, \quad (17)$$

$$s_k = -\nabla f|_{x_k} + \beta_k s_{k-1}, \quad (18)$$

with  $\beta_k$  defined in (16).

### 3.3.3. Quasi-Newton method

Upon differentiating the right hand side of (10), we see that its minimum is found at the points

$$y = -\mathcal{H}^f|_{x_k}^{-1}(\nabla f|_{x_k}), \quad (19)$$

given that  $\mathcal{H}^f|_{x_k}^{-1}$  exists. But  $\mathcal{H}^f|_{x_k}^{-1}$  is intractable in the present context, whether or not it exists. Yet, assuming that it does, the equation can be solved approximately using, e.g., standard CG for a quadratic cost functional, see [15] for details. This leads to an approximate Newton search direction  $s_k \approx -\mathcal{H}^f|_{x_k}^{-1}(\nabla f|_{x_k})$ , and a Quasi-Newton update  $x_{k+1} = x_k + \alpha_k s_k$ , with  $\alpha_k$  given by (14).

## 4. Gradient and Hessian, preliminary computations

Instead of writing out the expressions for the Hessians in full, we will rely on a nested scheme where  $f^G$  and  $f^P$  are written as a composition of a number of simpler functions, which are then combined to a full gradient and Hessian by the use of Theorem 1. This strategy allows us to arrive at simple, interpretable and easy to implement expressions for the gradient, the bilinear Hessian and the Hessian operator.



#### 4.1. Gaussian noise

In order to simplify the computation of the gradient and bilinear Hessian, we introduce the functional  $F^G : \mathbb{C}^{M \times M \times K} \rightarrow \mathbb{R}$

$$F^G(\Psi) = \sum_{\gamma \in \Gamma} w_\gamma \left( |\Psi_\gamma| - d_\gamma \right)^2, \quad (20)$$

where the modulus is applied pointwise. The point is that then we can set  $\Psi = D_K(I_K(q) \cdot S_r(\psi))$  so that

$$f^G(q, \psi) = F^G\left(D_K(I_K(q) \cdot S_r(\psi))\right)$$

and break up the computations in smaller pieces, following Theorem 1. We can then more easily also treat the situation with Poisson noise  $f^P$ , which we do in the next section.

Following [15], we will consider  $\mathbb{C}^{M \times M \times K}$  as a complex inner product space endowed with the usual inner product  $\langle u, v \rangle = \sum_\gamma u_\gamma \bar{v}_\gamma$  in  $\mathbb{C}^{M \times M \times K}$ , where  $\gamma$  runs over all possible multi-indices  $\gamma = (\gamma_1, \gamma_2, \gamma_3) \in \{1, \dots, M\}^2 \times \{1, \dots, K\}$ , and corresponding norm  $\|u\|^2 = \sum_\gamma |u_\gamma|^2$ . Note that this can also be considered as a linear space over  $\mathbb{R}$  by introducing the real inner product  $\langle u, v \rangle_{\mathbb{R}} = \text{Re}\langle u, v \rangle$ , which is crucial in order to be able to define gradients of the functionals  $f^G$  and  $f^P$ . We consider the former in this section and postpone the corresponding computations for  $f^P$  to the next.

To compute the gradient and bilinear Hessian of  $F^G$ , following the steps detailed in Procedure 1 from [15], we first use the Taylor expansion to derive

$$|z_0 + \Delta z| = |z_0| + \frac{\text{Re}(\bar{z}_0 \Delta z)}{|z_0|} + \frac{1}{2} \frac{|\Delta z|^2}{|z_0|} - \frac{1}{2} \frac{(\text{Re}(\bar{z}_0 \Delta z))^2}{|z_0|^3} + \mathcal{O}(|\Delta z|^3), \quad (21)$$

where  $z_0, \Delta z \in \mathbb{C}$ . We then insert this in the expression (20) to obtain

$$F^G(\Psi_0 + \Delta\Psi) = \left\| \sqrt{w} \cdot \left( |\Psi_0| - d + \text{Re} \left( \frac{\bar{\Psi}_0 \cdot \Delta\Psi}{|\Psi_0|} \right) + \frac{1}{2} \frac{|\Delta\Psi|^2}{|\Psi_0|} - \frac{1}{2} \frac{(\text{Re}(\bar{\Psi}_0 \cdot \Delta\Psi))^2}{|\Psi_0|^3} + \mathcal{O}(\|\Delta\Psi\|^3) \right) \right\|^2,$$

where all operations are applied elementwise and  $w$  denotes the tensor  $w = (w_\gamma)_{\gamma \in \Gamma}$ . Expanding the inner product and collecting higher-order combinations in the  $\mathcal{O}(\|\Delta\Psi\|^3)$ -term we find that

$$\begin{aligned} F^G(\Psi_0 + \Delta\Psi) &= \left\| \sqrt{w} \cdot (|\Psi_0| - d) \right\|^2 + 2\text{Re} \left\langle w \cdot (|\Psi_0| - d), \frac{\bar{\Psi}_0}{|\Psi_0|} \cdot \Delta\Psi \right\rangle + \\ &\left\| \sqrt{w} \cdot \left( \text{Re} \left( \frac{\bar{\Psi}_0 \cdot \Delta\Psi}{|\Psi_0|} \right) \right) \right\|^2 + \left\langle w \cdot (|\Psi_0| - d), \frac{|\Delta\Psi|^2}{|\Psi_0|} - \frac{(\text{Re}(\bar{\Psi}_0 \cdot \Delta\Psi))^2}{|\Psi_0|^3} \right\rangle + \mathcal{O}(\|\Delta\Psi\|^3) \\ &= F^G(\Psi_0) + 2\text{Re} \langle w \cdot (\Psi_0 - d \cdot \Psi_0 / |\Psi_0|), \Delta\Psi \rangle + \\ &\langle w - w \cdot d / |\Psi_0|, |\Delta\Psi|^2 \rangle + \left\langle w \cdot d / |\Psi_0|^3, (\text{Re}(\bar{\Psi}_0 \cdot \Delta\Psi))^2 \right\rangle + \mathcal{O}(\|\Delta\Psi\|^3) \end{aligned}$$

from which it immediately follows that

$$\nabla F^G|_{\Psi_0} = 2w \cdot (\Psi_0 - d \cdot \Psi_0 / |\Psi_0|). \quad (22)$$

Similarly, by the uniqueness of the Hessian we see that

$$\frac{1}{2} \mathcal{H}^{F^G}|_{\Psi_0}(\Delta\Psi, \Delta\Psi) = \langle w - w \cdot d / |\Psi_0|, |\Delta\Psi|^2 \rangle + \left\langle w \cdot d / |\Psi_0|^3, (\text{Re}(\bar{\Psi}_0 \cdot \Delta\Psi))^2 \right\rangle.$$

To obtain the Hessian as a symmetric bilinear form, one could use the polarization identity [15, Eq. (14)], but by simply looking at the expression it is clear that

$$\begin{aligned} \frac{1}{2} \mathcal{H}^{FG} |_{\Psi_0} (\Delta\Psi^{(1)}, \Delta\Psi^{(2)}) &= \left\langle w - w \cdot d/|\Psi_0|, \operatorname{Re}(\Delta\Psi^{(1)} \cdot \overline{\Delta\Psi^{(2)}}) \right\rangle + \\ &\left\langle w \cdot d/|\Psi_0|^3, \operatorname{Re}(\overline{\Psi_0} \cdot \Delta\Psi^{(1)}) \cdot \operatorname{Re}(\overline{\Psi_0} \cdot \Delta\Psi^{(2)}) \right\rangle \end{aligned}$$

is a symmetric bilinear form which coincides with the above on the “diagonal”  $\Delta\Psi^{(1)} = \Delta\Psi^{(2)} = \Delta\Psi$ , so by the uniqueness of such forms (see [15]), this must be the sought expression.

To arrive at the corresponding Hessian operator  $H^{FG} |_{\Psi_0}$ , which acts on  $\mathbb{C}^{M \times M \times K}$ , we first note that the bilinear Hessian can be written

$$\begin{aligned} \frac{1}{2} \mathcal{H}^{FG} |_{\Psi_0} (\Delta\Psi^{(1)}, \Delta\Psi^{(2)}) &= \operatorname{Re} \left\langle (w - w \cdot d/|\Psi_0|) \cdot \Delta\Psi^{(1)}, \Delta\Psi^{(2)} \right\rangle + \\ &\operatorname{Re} \left\langle w \cdot d \cdot \Psi_0/|\Psi_0|^3 \cdot \operatorname{Re}(\overline{\Psi_0} \cdot \Delta\Psi^{(1)}), \Delta\Psi^{(2)} \right\rangle \end{aligned} \quad (23)$$

from which it immediately follows that

$$H^{FG} |_{\Psi_0} (\Delta\Psi) = 2 \left( w - w \cdot \frac{d}{|\Psi_0|} \right) \cdot \Delta\Psi + 2w \cdot d \cdot \frac{\Psi_0}{|\Psi_0|^3} \cdot \operatorname{Re}(\overline{\Psi_0} \cdot \Delta\Psi). \quad (24)$$

#### 4.2. Poisson noise

In analogy with (20) we introduce the functional  $F^P : \mathbb{C}^{M \times M \times K} \rightarrow \mathbb{R}$  by setting

$$F^P(\Psi) = \sum_{\gamma \in \Gamma} w_\gamma \cdot \left( |\Psi_\gamma|^2 - 2d_\gamma^2 \log(|\Psi_\gamma|) \right). \quad (25)$$

Using that  $\log(x_0 + \Delta x) = \log(x_0) + \frac{\Delta x}{x_0} - \frac{1}{2} \frac{\Delta x^2}{x_0^2} + \mathcal{O}(\Delta x^3)$  we get, by inserting (21), that

$$\begin{aligned} \log(|z_0 + \Delta z|) &= \log(|z_0|) + \frac{\operatorname{Re}(\overline{z_0} \Delta z)/|z_0| + \frac{1}{2} |\Delta z|^2/|z_0| - \frac{1}{2} (\operatorname{Re}(\overline{z_0} \Delta z))^2/|z_0|^3}{|z_0|} \\ &- \frac{1}{2} \frac{(\operatorname{Re}(\overline{z_0} \Delta z)/|z_0|)^2}{|z_0|^2} + \mathcal{O}(|\Delta z|^3), \end{aligned}$$

which simplifies to

$$\log(|z_0 + \Delta z|) = \log(|z_0|) + \frac{\operatorname{Re}(\overline{z_0} \Delta z)}{|z_0|^2} + \frac{1}{2} \frac{|\Delta z|^2}{|z_0|^2} - \frac{(\operatorname{Re}(\overline{z_0} \Delta z))^2}{|z_0|^4} + \mathcal{O}(|\Delta z|^3).$$

Inserting this into (25) we get

$$\begin{aligned} F^P(\Psi_0 + \Delta\Psi) &= \sum_{\gamma \in \Gamma} w_\gamma \left( |\Psi_{0,i}|^2 + 2\operatorname{Re} \overline{\Psi_{0,i}} \Delta\Psi_\gamma + |\Delta\Psi_\gamma|^2 - \right. \\ &2d_\gamma^2 \left( \log(|\Psi_{0,i}|) + \frac{\operatorname{Re}(\overline{\Psi_{0,i}} \Delta\Psi_\gamma)}{|\Psi_{0,i}|^2} + \frac{1}{2} \frac{|\Delta\Psi_\gamma|^2}{|\Psi_{0,i}|^2} - \frac{(\operatorname{Re}(\overline{\Psi_{0,i}} \Delta\Psi_\gamma))^2}{|\Psi_{0,i}|^4} \right) + \mathcal{O}(\|\Delta\Psi\|^3) \Big) = \\ &F^P(\Psi_0) + 2\operatorname{Re} \left\langle w \cdot (\Psi_0 - d^2) \cdot \Psi_0/|\Psi_0|^2, \Delta\Psi \right\rangle + \\ &\sum_{\gamma \in \Gamma} \left( w_\gamma - w_\gamma \frac{d_\gamma^2}{|\Psi_{0,i}|^2} \right) |\Delta\Psi_\gamma|^2 + 2w_\gamma \frac{d_\gamma^2 (\operatorname{Re}(\overline{\Psi_{0,i}} \Delta\Psi_\gamma))^2}{|\Psi_{0,i}|^4} + \mathcal{O}(\|\Delta\Psi\|^3). \end{aligned}$$

From the penultimate line we see that

$$\nabla F^P|_{\Psi_0} = 2w \cdot \left( \Psi_0 - d^2 \cdot \Psi_0 / |\Psi_0|^2 \right) \quad (26)$$

and, reusing the ideas in the previous section, that the bilinear Hessian is given by

$$\begin{aligned} \frac{1}{2} \mathcal{H}^{FP}|_{\Psi_0}(\Delta\Psi^{(1)}, \Delta\Psi^{(2)}) &= \\ \sum_{\gamma \in \Gamma} \left( w_\gamma - w_\gamma \frac{d_\gamma^2}{|\Psi_{0,i}|^2} \right) \operatorname{Re} \left( \Delta\Psi_\gamma^{(1)} \cdot \overline{\Delta\Psi_\gamma^{(2)}} \right) &+ 2w_\gamma \frac{d_\gamma^2 \operatorname{Re} \left( \overline{\Psi_{0,i}} \cdot \Delta\Psi_\gamma^{(1)} \right) \operatorname{Re} \left( \overline{\Psi_{0,i}} \Delta\Psi_\gamma^{(2)} \right)}{|\Psi_{0,i}|^4} = \\ \operatorname{Re} \left\langle \left( w - w \cdot \frac{d^2}{|\Psi_0|^2} \right) \cdot \Delta\Psi^{(1)}, \Delta\Psi^{(2)} \right\rangle &+ \operatorname{Re} \left\langle 2w \cdot \frac{d^2 \cdot \Psi_0 \cdot \operatorname{Re} \left( \overline{\Psi_0} \cdot \Delta\Psi^{(1)} \right)}{|\Psi_0|^4}, \Delta\Psi^{(2)} \right\rangle. \end{aligned} \quad (27)$$

Finally, we clearly also have that the Hessian operator  $H^{FP}|_{\Psi_0}$  is given by

$$H^{FP}|_{\Psi_0}(\Delta\Psi) = 2 \left( w - w \cdot \frac{d^2}{|\Psi_0|^2} \right) \cdot \Delta\Psi + 4w \cdot \frac{d^2 \cdot \Psi_0 \cdot \operatorname{Re} \left( \overline{\Psi_0} \cdot \Delta\Psi \right)}{|\Psi_0|^4}. \quad (28)$$

## 5. The gradient and the bilinear Hessian

In this section we return to the functionals  $f^G$  and  $f^P$  as defined in (4) and (5), and show how to derive the bilinear Hessian along with all gradients in order to, e.g., be able to make a quadratic approximation of the graph at any given point. More precisely, we consider the functional

$$f(q, \psi) = F \left( D_K(I_K(q) \cdot S_r(\psi)) \right)$$

where  $q$  and  $\psi$  are the variables and  $f, F$  denotes either  $f^G, F^G$  or  $f^P, F^P$ , respectively. One could also consider the positions  $r$  as variables, and in practice this is necessary for good reconstructions, but for simplicity of exposition we add this layer of complexity in Section 7.

In order to define the gradient and bilinear Hessian of  $f$  using the abstract framework from Section 3.1, we recall the construction of “direct sum” of inner product spaces, and note that  $(q, \psi)$  naturally become variables in the space  $\mathbb{X} = \mathbb{C}^{M \times M} \oplus \mathbb{C}^{N \times N}$ , where  $\oplus$  denotes the direct sum, i.e. the linear space  $\mathbb{C}^{M \times M} \times \mathbb{C}^{N \times N}$  endowed with the “natural” scalar product

$$\langle (q_1, \psi_1), (q_2, \psi_2) \rangle_{\mathbb{X}} = \langle q_1, q_2 \rangle_{\mathbb{C}^{M \times M}} + \langle \psi_1, \psi_2 \rangle_{\mathbb{C}^{N \times N}}.$$

This is precisely the scalar product one would get if we were to column-stack and concatenate  $(q, \psi)$  and identify it with an element of  $\mathbb{C}^n$  with  $n = M^2 + N^2$ .

To clarify computations lets introduce the new variables  $a = I_K(q)$  and  $b = S_r(\psi)$ . We introduce the auxiliary function  $\mathcal{L} : (\mathbb{C}^{M \times M \times K})^2 \rightarrow \mathbb{C}^{M \times M \times K}$  defined as  $\mathcal{L}(a, b) = D_K(a \cdot b)$  so that

$$f(q, \psi) = F \left( \mathcal{L}(I_K(q), S_r(\psi)) \right). \quad (29)$$

where  $(\mathbb{C}^{M \times M \times K})^2$  is short for  $\mathbb{C}^{M \times M \times K} \oplus \mathbb{C}^{M \times M \times K}$ . By linearity of  $D_K$  it follows that

$$\mathcal{L}(a_0 + \Delta a, b_0 + \Delta b) = \mathcal{L}(a_0, b_0) + D_K(\Delta a \cdot b_0 + a_0 \cdot \Delta b + \Delta a \cdot \Delta b).$$

The two middle terms give that

$$d\mathcal{L}|_{(a_0, b_0)}(\Delta a, \Delta b) = D_K(\Delta a \cdot b_0 + a_0 \cdot \Delta b)$$

whereas the latter yields

$$d^2 \mathcal{L}|_{(a_0, b_0)}((\Delta a, \Delta b), (\Delta a, \Delta b)) = 2D_K(\Delta a \cdot \Delta b)$$

where the factor 2 comes from the fact that  $d^2 \mathcal{L}$  has a factor  $\frac{1}{2}$  in front of it, see Definition 6. By the uniqueness part of Theorem 1 in [15], the bilinear version of  $d^2 \mathcal{L}$  must thus be

$$d^2 \mathcal{L}|_{(a_0, b_0)}((\Delta a^{(1)}, \Delta b^{(1)}), (\Delta a^{(2)}, \Delta b^{(2)})) = D_K(\Delta a^{(1)} \cdot \Delta b^{(2)} + \Delta a^{(2)} \cdot \Delta b^{(1)})$$

since this is a symmetric bilinear form which coincides with the former expression on the “diagonal”  $\Delta a^{(1)} = \Delta a^{(2)}, \Delta b^{(1)} = \Delta b^{(2)}$ .

Finally, we want to compose everything to get the gradient and bilinear Hessian for  $f$ . Setting  $a_0 = I_K(q_0)$ ,  $\Delta a = I_K(\Delta q)$ ,  $b_0 = S_r(\psi_0)$  and  $\Delta b = S_r(\Delta \psi)$  we get, following formula (8) and (11), that  $\text{Re}\langle \nabla f|_{(q_0, \psi_0)}, (\Delta q, \Delta \psi) \rangle_{\mathbb{C}^{M \times M \times K} \oplus \mathbb{C}^{N \times N}}$  equals

$$\begin{aligned} & \text{Re}\left\langle \nabla F|_{\mathcal{L}(a_0, b_0)}, d\mathcal{L}|_{(a_0, b_0)}(I_K(\Delta q), S_r(\Delta \psi)) \right\rangle_{\mathbb{C}^{M \times M \times K}} = \\ & \text{Re}\left\langle D_K^*(\nabla F|_{\mathcal{L}(a_0, b_0)}), I_K(\Delta q) \cdot b_0 + a_0 \cdot S_r(\Delta \psi) \right\rangle_{\mathbb{C}^{M \times M \times K}}, \end{aligned}$$

where we explicitly indicate which scalar product is referred to for extra clarity. Here,  $D_K^*$  denotes the operator adjoint of  $D_K$  and is simply the standard adjoint  $D^*$  applied individually to each of the  $K$  data slices in  $\mathbb{C}^{M \times M \times K}$ . To shorten notation, we introduce

$$\Phi_0 = D_K^*(\nabla F|_{\mathcal{L}(q_0, \psi_0)}). \quad (30)$$

Summing up we see that

$$\begin{aligned} & \text{Re}\langle \nabla f|_{(q_0, \psi_0)}, (\Delta q, \Delta \psi) \rangle_{\mathbb{C}^{M \times M} \oplus \mathbb{C}^{N \times N}} = \\ & \text{Re}\langle I_K^*(\overline{b_0} \Phi_0), \Delta q \rangle_{\mathbb{C}^{M \times M}} + \text{Re}\langle S_r^*(\overline{a_0} \Phi_0), \Delta \psi \rangle_{\mathbb{C}^{N \times N}} = \\ & \text{Re}\left\langle (I_K^*(\overline{S_r(\psi_0)} \Phi_0), S_r^*(\overline{I_K(q_0)} \Phi_0)), (\Delta q, \Delta \psi) \right\rangle_{\mathbb{C}^{M \times M} \oplus \mathbb{C}^{N \times N}} \end{aligned}$$

where  $I_K^*$ , as noted in Section 2, is simply an operator summing over the third index. By definition (8) (with  $\mathbb{X} = \mathbb{C}^{M \times M} \oplus \mathbb{C}^{N \times N}$ ), we see that

$$\nabla f|_{(q_0, \psi_0)} = \left( I_K^*(\overline{S_r(\psi_0)} \Phi_0), S_r(\overline{I_K(q_0)} \Phi_0) \right) \quad (31)$$

or equivalently that  $\nabla_q f|_{(q_0, \psi_0)} = I_K^*(\overline{S_r(\psi_0)} \Phi_0)$  and  $\nabla_\psi f|_{(q_0, \psi_0)} = S_r(\overline{I_K(q_0)} \Phi_0)$ . Turning now to the Hessian as a bilinear form, applying (12) to (29) (and as before setting  $a_0 = I_K(q_0)$  and  $b_0 = S_r(\psi_0)$ ) gives

$$\begin{aligned} & \mathcal{H}^f|_{(q_0, \psi_0)}\left((\Delta q^{(1)}, \Delta \psi^{(1)}), (\Delta q^{(2)}, \Delta \psi^{(2)})\right) = \\ & \text{Re}\left\langle \Phi_0, d^2 \mathcal{L}|_{(a_0, b_0)}\left((I_K(\Delta q^{(1)}), S_r(\Delta \psi^{(1)})), (I_K(\Delta q^{(2)}), S_r(\Delta \psi^{(2)}))\right)\right\rangle + \\ & \mathcal{H}^F|_{\mathcal{L}(a_0, b_0)}\left(d\mathcal{L}|_{(a_0, b_0)}(I_K(\Delta q^{(1)}), S_r(\Delta \psi^{(1)})), d\mathcal{L}|_{(a_0, b_0)}(I_K(\Delta q^{(2)}), S_r(\Delta \psi^{(2)}))\right) \end{aligned}$$

where  $\mathcal{H}^F$  is given in the end of Section 4.1 or 4.2, depending on whether the noise is Gaussian or Poisson.

To wrap up, we have collected formulas for all partial derivatives and the bilinear Hessian, without explicitly differentiating a single time. The resulting expressions, when relying on the chain rule as above, are straightforward to implement and fast to execute, with all operators acting

directly in matrix or tensor space. Armed with this, we can now approximate the graph of  $f$  near a given point  $x_0 = (q_0, \psi_0)$ , via

$$f(x) \approx f(x_0) + \langle \nabla_x f|_{x_0}, x - x_0 \rangle + \frac{1}{2} \mathcal{H}^f|_{x_0}(x - x_0, x - x_0)$$

where  $\langle \nabla_x f|_{x_0}, x - x_0 \rangle$  can be broken up into

$$\langle \nabla_x f|_{x_0}, x - x_0 \rangle = \text{Re} \langle \nabla_q f|_{x_0}, q - q_0 \rangle + \text{Re} \langle \nabla_\psi f|_{x_0}, \psi - \psi_0 \rangle.$$

## 6. The Hessian operator

In order to implement second order solvers such as Newton's method, the bilinear Hessian is not enough but we also need the "Hessian operator". In this section we show how to retrieve an operator  $H^f|_{(q_0, \psi_0)} : \mathbb{C}^{M \times M} \oplus \mathbb{C}^{N \times N} \rightarrow \mathbb{C}^{M \times M} \oplus \mathbb{C}^{N \times N}$  such that

$$\mathcal{H}^f|_{(q_0, \psi_0)} \left( (\Delta q^{(1)}, \Delta \psi^{(1)}), (\Delta q^{(2)}, \Delta \psi^{(2)}) \right) = \left\langle H^f|_{(q_0, \psi_0)} (\Delta q^{(1)}, \Delta \psi^{(1)}), (\Delta q^{(2)}, \Delta \psi^{(2)}) \right\rangle.$$

Since the bilinear Hessian is symmetric, the operator is also symmetric. Note that, if we were to arrange all the elements of  $\mathbb{C}^{M \times M} \oplus \mathbb{C}^{N \times N}$  in a column vector and separate the real and imaginary parts, thereby identifying  $\mathbb{C}^{M \times M} \oplus \mathbb{C}^{N \times N}$  with  $\mathbb{R}^{2M^2+2N^2}$ , then  $H^f|_{(q_0, \psi_0)}$  would really be the traditional Hessian matrix  $\mathbf{H}^f|_{(q_0, \psi_0)}$ . Also note that it naturally would split up into 4 submatrices

$$\begin{pmatrix} \mathbf{H}_{11}^f & \mathbf{H}_{12}^f \\ \mathbf{H}_{21}^f & \mathbf{H}_{22}^f \end{pmatrix} \quad (32)$$

where  $\mathbf{H}_{11}^f$  sends  $q$ -variables into new  $q$ -variables,  $\mathbf{H}_{12}^f$  sends  $\psi$ -variables into  $q$ -variables and so on. By symmetry we would also have  $\mathbf{H}_{21}^f = \mathbf{H}_{12}^{f^t}$ . In a similar manner, we will find 4 operators  $H_{11}^f, H_{12}^f$  etc. with corresponding roles, but acting on  $\mathbb{C}^{M \times M}$  and  $\mathbb{C}^{N \times N}$  directly. These will be given by efficiently implementable rules and we shall have that  $H_{21}^f$  is the adjoint of  $H_{12}^f$  (with respect to the real scalar product on the respective spaces).

**Theorem 2** *The Hessian operator  $H^f|_{(q_0, \psi_0)}(\Delta q, \Delta \psi)$  can be computed by the following steps:*

- Compute  $\Phi_0 = D_K^*(\nabla F|_{\mathcal{L}(q_0, \psi_0)})$  (recall (30)).
- Compute  $\Xi_0(\Delta q, \Delta \psi) = D_K^* \left( H^F|_{\mathcal{L}(q_0, \psi_0)} \left( D_K(I_K(\Delta q) \cdot S_r(\psi_0) + I_K(q_0) \cdot S_r(\Delta \psi)) \right) \right)$
- Compute  $A_1 = I_K^* \left( \overline{S_r(\Delta \psi)} \cdot \Phi_0 + \overline{S_r(\psi_0)} \cdot \Xi_0(\Delta q, \Delta \psi) \right)$
- Compute  $A_2 = S_r^* \left( \overline{I_K(\Delta q)} \cdot \Phi_0 + \overline{I_K(q_0)} \cdot \Xi_0(\Delta q, \Delta \psi) \right)$
- Set  $H^f|_{(q_0, \psi_0)} = (A_1, A_2)$ .

*Proof:* By combining formulas of Section 4.1 and 5 we see that the bilinear Hessian is given by

$$\begin{aligned}
& \mathcal{H}^{FG} |_{(q_0, \psi_0)} \left( (\Delta q^{(1)}, \Delta \psi^{(1)}), (\Delta q^{(2)}, \Delta \psi^{(2)}) \right) = \\
& \operatorname{Re} \left\langle \Phi_0, I_K(\Delta q^{(1)}) \cdot S_r(\Delta \psi^{(2)}) + I_K(\Delta q^{(2)}) \cdot S_r(\Delta \psi^{(1)}) \right\rangle + \\
& \operatorname{Re} \left\langle H^{FG} |_{\mathcal{L}(q_0, \psi_0)} \left( D_K(I_K(\Delta q^{(1)}) \cdot S_r(\psi_0) + I_K(q_0) \cdot S_r(\Delta \psi^{(1)})) \right), \right. \\
& \quad \left. D_K(I_K(\Delta q^{(2)}) \cdot S_r(\psi_0) + I_K(q_0) \cdot S_r(\Delta \psi^{(2)})) \right\rangle = \\
& \operatorname{Re} \left\langle \Phi_0, I_K(\Delta q^{(1)}) \cdot S_r(\Delta \psi^{(2)}) + I_K(\Delta q^{(2)}) \cdot S_r(\Delta \psi^{(1)}) \right\rangle + \\
& \quad \left\langle \Xi_0(\Delta q^{(1)}, \Delta \psi^{(1)}), I_K(\Delta q^{(2)}) \cdot S_r(\psi_0) + I_K(q_0) \cdot S_r(\Delta \psi^{(2)}) \right\rangle = \\
& \operatorname{Re} \left\langle \overline{I_K(\Delta q^{(1)})} \cdot \Phi_0 + \overline{I_K(q_0)} \cdot \Xi_0(\Delta q^{(1)}, \Delta \psi^{(1)}), S_r(\Delta \psi^{(2)}) \right\rangle + \\
& \quad \left\langle \overline{S_r(\Delta \psi^{(1)})} \cdot \Phi_0 + \overline{S_r(\psi_0)} \cdot \Xi_0(\Delta q^{(1)}, \Delta \psi^{(1)}), I_K(\Delta q^{(2)}) \right\rangle
\end{aligned}$$

where  $\Phi_0 = D_K^*(\nabla F|_{\mathcal{L}(q_0, \psi_0)})$ .  $\square$

We remark that if we consider the probe as fixed and only compute the Hessian operator related to  $\psi$  (i.e. we insert  $(0, \Delta \psi)$  above and only compute  $A_2$ , which is the operator corresponding to the matrix  $\mathbf{H}_{22}^f$  had we vectorized), then the formula in Theorem 2 reduces to

$$S_r^* \left( \overline{I_K(q_0)} \cdot D_K^* \left( H^F |_{\mathcal{L}(q_0, \psi_0)} \left( D_K(I_K(q_0) \cdot S_r(\Delta \psi)) \right) \right) \right). \quad (33)$$

Analogous formulas have been computed in matrix form in [11], see Appendix A. In particular, upon inserting formula (24) for  $H^F$  in the above expression we retrieve the analogue of (42) from [11], and by inserting (28) we get (44) of the same paper. Clearly, relying on (33) is much “cleaner” implementation-wise and many orders of magnitude faster to evaluate. Indeed, the numerical experiments in [11] are performed on  $32 \times 32$  matrices, whereas our methods easily handle  $2048 \times 2048$  images.

## 7. The bilinear Hessian for ptychography with position correction

In this section we return to the objective functionals  $f^G$  and  $f^P$  as defined in (4) and (5) but modified so that also the positions  $r$  are considered as unknowns. As before we drop the superscript  $G$  or  $P$  for simplicity. Moreover, we will simply add  $r$  as an independent variable so by slight abuse of notation we write  $f(q, \psi, r)$ , where

$$f(q, \psi, r) = F(\mathcal{L}(I_K(q), S_r(\psi))) \quad (34)$$

just like in (29). The shifting takes place in the Fourier domain and is defined, for each slice  $(S_r(\psi))_k$ ,  $k = 1, \dots, K$ , as

$$(S_r(\psi))_k = C(\mathcal{F}^{-1}(e^{-ir_k \cdot \xi} \hat{\psi}(\xi)))$$

where  $\mathcal{F}$  denotes the (discrete) Fourier transform and  $C$  is an operator which crops the full image  $\mathbb{C}^{N \times N}$  to a smaller central piece  $\mathbb{C}^{M \times M}$ . It will be convenient to think of the above operator also as a function of  $r_k$  so therefore we introduce  $T_\psi : \mathbb{R}^2 \rightarrow \mathbb{C}^{M \times M}$  defined by

$$T_\psi(z) := C(\mathcal{F}^{-1}(e^{-iz \cdot \xi} \hat{\psi}(\xi))).$$

We thus have  $S_r(\psi) = (T_\psi(r_k))_{k=1}^K$ ; though this introduces two notations for essentially the object, it will significantly simplify the upcoming computations.

We first expand  $T_\psi(z)$  in a Taylor-series with respect to a perturbation  $\Delta z$  of some fixed  $z_0$ ; Since

$$e^{-i(z_0+\Delta z)\cdot\xi} = e^{-iz_0\cdot\xi} \left( 1 - i\Delta z \cdot \xi + \frac{(-i)^2}{2}(\Delta z \cdot \xi)^2 + \mathcal{O}(\|\Delta z\|^3) \right)$$

we get that

$$T_\psi(z_0 + \Delta z) = C(\mathcal{F}^{-1}(e^{-iz_0\cdot\xi} \left( 1 - i(\Delta z \cdot \xi) - \frac{1}{2}(\Delta z \cdot \xi)^2 + \mathcal{O}(\|\Delta z\|^3) \right) \hat{\psi}(\xi))).$$

Comparing this expression with (6) we see that

$$dT_\psi|_{z_0}(\Delta z) = -i C \left( \mathcal{F}^{-1}((\Delta z \cdot \xi) e^{-iz_0\cdot\xi} \hat{\psi}(\xi)) \right) \quad (35)$$

and

$$d^2T_\psi|_{z_0}(\Delta z, \Delta z) = -C \left( \mathcal{F}^{-1}((\Delta z \cdot \xi)^2 e^{-iz_0\cdot\xi} \hat{\psi}(\xi)) \right).$$

Since later we will also need the bilinear version of this, we remark already that

$$d^2T_\psi|_{z_0}(\Delta z, \Delta w) = -C(\mathcal{F}^{-1}((\Delta z \cdot \xi)(\Delta w \cdot \xi) e^{-iz_0\cdot\xi} \hat{\psi})), \quad (36)$$

which is clearly real bilinear and symmetric, so by uniqueness of such objects it must be the one sought.

Since the operator  $T_\psi$  is linear in the  $\psi$ -variable, we get that the joint expansion for a perturbation  $T_{\psi_0+\Delta\psi}(z_0 + \Delta z)$  considered as a function on  $\mathbb{C}^{N \times N} \times \mathbb{R}^2$  becomes

$$\begin{aligned} T_{\psi_0+\Delta\psi}(z_0 + \Delta z) &= T_{\psi_0}(z_0) + T_{\Delta\psi}(z_0) + dT_{\psi_0}|_{z_0}(\Delta z) + dT_{\Delta\psi}|_{z_0}(\Delta z) \\ &\quad + \frac{1}{2} \left( d^2T_\psi|_{z_0}(\Delta z, \Delta z) \right) + \mathcal{O}(\|(\Delta\psi, \Delta z)\|^3). \end{aligned}$$

Note that the first order terms are collected on the first row, whereas the second row contain the second order terms and the order. We now consider the function  $\mathcal{S} : \mathbb{C}^{N \times N} \times (\mathbb{R}^2)^K \rightarrow \mathbb{C}^{M \times M \times K}$  defined as

$$\mathcal{S}(\psi, r) = S_r(\psi) = (T_\psi(r_k))_{k=1}^K,$$

where  $r = (r_1, \dots, r_K)$  and each  $r_k \in \mathbb{R}^2$ . By the linear part of the penultimate equation we have that

$$d\mathcal{S}|_{(\psi_0, r_0)}(\Delta\psi, \Delta r) = \left( (T_{\Delta\psi}(r_{0,k}) + dT_{\psi_0}|_{r_{0,k}}(\Delta r_k)) \right)_{k=1}^K = S_{r_0}(\Delta\psi) + \left( dT_{\psi_0}|_{r_{0,k}}(\Delta r_k) \right)_{k=1}^K$$

and the bottom row gives

$$d^2\mathcal{S}|_{(\psi_0, r_0)}((\Delta\psi, \Delta r), (\Delta\psi, \Delta r)) = \left( 2dT_{\Delta\psi}|_{r_{0,k}}(\Delta r_k) + d^2T_\psi|_{r_{0,k}}(\Delta r_k, \Delta r_k) \right)_{k=1}^K$$

where  $d^2T_\psi|_{r_{0,k}}$  is given in (36). The bilinear version is now straightforward to get

$$\begin{aligned} d^2\mathcal{S}|_{(\psi_0, r_0)}((\Delta\psi^{(1)}, \Delta r^{(1)}), (\Delta\psi^{(2)}, \Delta r^{(2)})) &= \\ & \left( dT_{\Delta\psi^{(1)}}|_{r_{0,k}}(\Delta r_k^{(2)}) + dT_{\Delta\psi^{(2)}}|_{r_{0,k}}(\Delta r_k^{(1)}) + d^2T_\psi|_{r_0}(\Delta r_k^{(1)}, \Delta r_k^{(2)}) \right)_{k=1}^K. \end{aligned}$$

Finally, we want to compose everything to get the gradient and bilinear Hessian for the function  $f$  in (34), which now can be written  $f(q, \psi, r) = (f \circ \mathcal{L})(q, \mathcal{S}(\psi, r))$ . Introducing, as in Section

5  $a = I_K(q)$  and  $b = \mathcal{S}(\psi, r)$  and following the computations there (see the computation before (30) for the linear term and the one following (31) for the quadratic term), we see that

$$\begin{aligned} (f \circ \mathcal{L})(a_0 + \Delta a, b_0 + \Delta b) &= (f \circ \mathcal{L})(a_0, b_0) + \operatorname{Re} \left\langle \Phi_0, d\mathcal{L}|_{(a_0, b_0)}(\Delta a, \Delta b) \right\rangle + \\ &\frac{1}{2} \operatorname{Re} \left\langle \Phi_0, d^2\mathcal{L}|_{(a_0, b_0)}((\Delta a, \Delta b)^{\times 2}) \right\rangle + \frac{1}{2} \mathcal{H}^F|_{\mathcal{L}(a_0, b_0)} \left( (d\mathcal{L}|_{(a_0, b_0)}(\Delta a, \Delta b))^{\times 2} \right) + \mathcal{O}(\|(\Delta a, \Delta b)\|^3) \\ &= f(q_0, \psi_0, r_0) + \operatorname{Re} \left\langle \Phi_0, \Delta a \cdot b_0 + a_0 \cdot \Delta b \right\rangle + \frac{1}{2} \mathcal{H}^{f \circ \mathcal{L}}|_{(a_0, b_0)} \left( (\Delta a, \Delta b)^{\times 2} \right) + \mathcal{O}(\|(\Delta a, \Delta b)\|^3) \end{aligned}$$

where  $\mathcal{H}^F$  is given in the end of Section 4.1 and 4.2 for Gaussian or Poisson noise, respectively. Above  $((\Delta a, \Delta b), (\Delta a, \Delta b))$  stands for  $(\Delta a, \Delta b)^{\times 2}$ , and

$$\begin{aligned} \mathcal{H}^{f \circ \mathcal{L}}|_{(a_0, b_0)} \left( (\Delta a, \Delta b)^{\times 2} \right) &:= \\ &\operatorname{Re} \left\langle \Phi_0, d^2\mathcal{L}|_{(a_0, b_0)}((\Delta a, \Delta b)^{\times 2}) \right\rangle + \mathcal{H}^F|_{\mathcal{L}(a_0, b_0)} \left( (d\mathcal{L}|_{(a_0, b_0)}(\Delta a, \Delta b))^{\times 2} \right). \end{aligned}$$

We now insert  $\Delta a = I_K(\Delta q)$ , similar to what we did in Section 5, but we put

$$\Delta b = d\mathcal{S}|_{(\psi_0, r_0)}(\Delta\psi, \Delta r) + \frac{1}{2} d^2\mathcal{S}|_{(\psi_0, r_0)}((\Delta\psi, \Delta r)^{\times 2})$$

in place of  $S_r(\Delta\psi)$ . Just as in the proof of Theorem 1 we then see that the second order Taylor expansion of  $f(q_0 + \Delta q, \psi_0 + \Delta\psi, r_0 + \Delta r) = (f \circ \mathcal{L})(q_0 + \Delta q, \mathcal{S}(\psi_0 + \Delta\psi, r_0 + \Delta r))$  becomes

$$\begin{aligned} f(q_0, \psi_0, r_0) + \operatorname{Re} \left\langle \Phi_0, I_K(\Delta q) \cdot b_0 + a_0 \cdot \left( d\mathcal{S}|_{(\psi_0, r_0)}(\Delta\psi, \Delta r) + \frac{1}{2} d^2\mathcal{S}|_{(\psi_0, r_0)}((\Delta\psi, \Delta r)^{\times 2}) \right) \right\rangle \\ + \frac{1}{2} \mathcal{H}^{f \circ \mathcal{L}}|_{(a_0, b_0)} \left( (I_K(\Delta q), d\mathcal{S}|_{(\psi_0, r_0)}(\Delta\psi, \Delta r))^{\times 2} \right) + \mathcal{O}(\|(\Delta q, \Delta\psi, \Delta r)\|^3) \end{aligned}$$

where we omitted the  $d^2\mathcal{S}$ -term from the second row since this part anyways gets absorbed by the ordo (as in the proof of Theorem 1).

From the above expression we can now easily identify the gradient and the bilinear Hessian. Obviously, the gradients  $\nabla_q f$  and  $\nabla_\psi f$  are the same as in (31) in Section 5, so we will not derive them again. Recalling (35) and the expression for  $d\mathcal{S}$ , we have that the term that depends linearly on  $\Delta r$  is

$$\begin{aligned} \operatorname{Re} \left\langle \Phi_0, a_0 \cdot \left( dT_{\psi_0}|_{r_{0,k}}(\Delta r_k) \right)_{k=1}^K \right\rangle &= \operatorname{Re} \left\langle \Phi_0, I_K(q_0) \cdot \left( dT_{\psi_0}|_{r_{0,k}}(\Delta r_k) \right)_{k=1}^K \right\rangle = \\ \operatorname{Re} \left\langle \Phi_0, -i \left( q_0 \cdot C(\mathcal{F}^{-1}(\xi_1 e^{r_{0,k} \cdot \xi} \hat{\psi}_0)) \Delta r_{k,1} + q_0 \cdot C(\mathcal{F}^{-1}(\xi_2 e^{r_{0,k} \cdot \xi} \hat{\psi}_0)) \Delta r_{k,2} \right)_{k=1}^K \right\rangle \end{aligned}$$

where  $(\Delta r_{k,1}, \Delta r_{k,2}) := \Delta r_k$ , from which it follows that  $\nabla_r f|_{(q_0, \psi_0, r_0)}$  equals

$$-\operatorname{Im} \left( \left( \left\langle \Phi_{0,k}, q_0 \cdot C(\mathcal{F}^{-1}(\xi_1 e^{r_{0,k} \cdot \xi} \hat{\psi}_0)) \right\rangle, \left\langle \Phi_{0,k}, q_0 \cdot C(\mathcal{F}^{-1}(\xi_2 e^{r_{0,k} \cdot \xi} \hat{\psi}_0)) \right\rangle \right)_{k=1}^K \right),$$

where we use  $\Phi_{0,k}$  to denote the  $k$ -th slice of  $\Phi_0$ . Note that the latter is a vector in  $(\mathbb{R}^2)^K$  and that the only difference between the formula for the first and second coordinate is the swapping of  $\xi_1$  for  $\xi_2$ . Turning finally to the Hessian (on the ‘‘diagonal’’) we have

$$\begin{aligned} \mathcal{H}^f|_{(q_0, \psi_0, r_0)}((\Delta q, \Delta\psi, \Delta r)^{\times 2}) &= \\ \operatorname{Re} \left\langle \Phi_0, d^2\mathcal{S}|_{(\psi_0, r_0)}((\Delta\psi, \Delta r)^{\times 2}) \right\rangle &+ \mathcal{H}^{f \circ \mathcal{L}}|_{(a_0, b_0)} \left( (I_K(\Delta q), d\mathcal{S}|_{(\psi_0, r_0)}(\Delta\psi, \Delta r))^{\times 2} \right), \end{aligned}$$

and the corresponding expression for the bilinear form immediately follows.



## 8. Numerical experiments and results

In this section, we evaluate our approach using both synthetic and experimental data reconstructions and compare the results to a couple of existing methods. We note that in this work our goal is to introduce and share the new method and do not perform a detailed comparison to all analogs. Also, although all provided formula derivations are valid for both near and far ptychography, our simulations are done only for near-field ptychography. We admit that there exist plenty of other reconstruction methods in ptychography, and all of them may behave differently for different datasets. We therefore defer a detailed comparison to future work.

We compare the convergence behavior and reconstruction results of the proposed BH-GD, BH-CG, and BH-QN methods, state-of-the-art Least Squares Maximum Likelihood (LSQML) [16] method, and popular nowadays Automatic Differentiation, with Adam optimizer [19], referred to as "Adam" in this paper, in analogy with the referenced work. LSQML is a generalized ptychography approach that optimizes the reconstruction along multiple directions, simultaneously optimizing the object, probe, and positions. It employs an optimized strategy to calculate the step length in the gradient descent direction for each variable, avoiding the need for computationally expensive line search procedures. The authors have demonstrated that LSQML outperforms analogs like ePIE [27] and Difference Map (DM) [28].

Comparison with the Adam approach is made as a reference for performance evaluation. Automatic Differentiation, particularly with Adam optimizer, is versatile and user-friendly, as it only requires formulas for the forward model, making it suitable for problems of varying complexity. However, it demands substantial computational resources, which can result in significantly slower performance compared to other methods. While Automatic Differentiation can potentially be used to extract second-order information, as demonstrated, e.g., in [15], it significantly increases the computational load and poses challenges for fitting data to GPUs, making it impractical for handling large datasets.

Reconstruction using different methods was performed within the same framework, employing identical forward and adjoint Fresnel transform operators, shift operators, and other computational components. "The methods were initially tested with various parameters, and those yielding optimal convergence behavior and reconstructions were selected to generate the final convergence plots and reconstructions for comparison with other methods. All methods were implemented in Python, with GPU acceleration. NVIDIA Tesla A100 was used for conducting performance tests.

### 8.1. Synthetic data: object and probe retrieval

As a synthetic data example, we generated an object based on the commonly used Siemens star sample, which is often employed at synchrotron beamlines to test spatial resolution. The phase component of the generated object is shown in the top-left corner of Figure 4. The amplitude component is 30 times lower. The object was created as a set of triangles with gaps at varying distances from the origin. To increase the complexity of the object, we randomly inserted sharp rectangles of different sizes within the star's segments. Additionally, we introduced low-frequency components in the background, as recovering these components may be more challenging in near-field ptychography.

The data modeling settings are shown in the left panel of Figure 2, replicating real-world parameters commonly encountered when working with experimental data. For the probe, we used a previous probe reconstruction from experimental data acquired at beamline ID16A of the ESRF. The amplitude and phase of the probe are displayed in the right panel of Figure 2. We note that the probe exhibits prominent vertical and horizontal components due to the structure of multilayered KB mirrors. The data were modeled for 16 object positions chosen based on the strategy described in [1]. Additionally, a small amount of Gaussian noise was added to the simulated data.

The reconstruction involved simultaneous recovery of both the object and probe using different

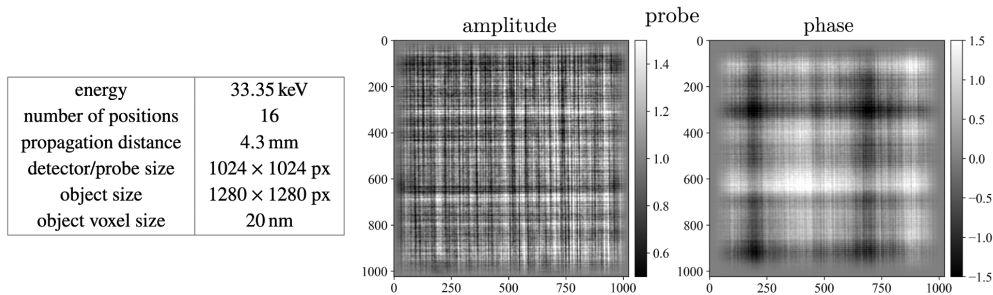


Fig. 2. Settings and the probe for near-field ptychography simulations.

methods. In this test, we chose to omit position correction procedures, as these are implemented differently across various packages and often function as independent supplementary steps, separate from the optimization of the object and probe. As an initial estimate for reconstructing the sample transmittance function  $\psi$ , we used the reconstruction generated by the Transport of Intensity Equation (TIE) method [29, 30], often referred to as the Paganin method in synchrotron beamline applications. This method was applied to the data after normalization by the reference image (i.e., data acquired without a sample). It is important to note that the Paganin method generally struggles to recover high-frequency components. As a result, the presence of horizontal and vertical line artifacts in the data due to the probe shape does not significantly affect the reconstruction quality. For the initial estimate of the probe function  $q$ , we used the square root of the reference image propagated back to the sample plane.

Figure 3 shows convergence plots for the objective functional value over 1000 iterations, using different optimization methods. In the left plot, the x-axis represents the iteration number, while the x-axis in the right plot is time (in seconds) for a fair performance comparison between methods. Both plots feature insets that allow for a detailed analysis of the algorithm’s behavior at the beginning, during iterations 5 to 70.

Within the illuminated region, all reconstruction methods converge to an approximation of the ground truth object, with numerical precision achieved after approximately 20000 iterations for slow methods. For demonstration purposes, we compare the reconstruction results each algorithm produces after 6 seconds of execution. During this time, the algorithms perform different numbers of iterations. For instance, BH-QN completes about 20 iterations, while BH-GD completes around 120 iterations. Figure 4 shows the corresponding reconstruction after 6 seconds of execution. The corresponding states of the objective functional are marked by the "visualization" line in the right panel of Figure 3. For reference, the reconstructed probe after 6 seconds using the BH-CG method is shown in Figure 5,a.

Several key observations can be made from these simulations. First, the second-order methods, BH-QN and BH-CG, outperform the others by a factor of at least 8-10. The reconstruction quality after 6 seconds of iterative scheme execution is significantly better for the second-order methods, as evidenced by the inset regions in Figure 4. This is further confirmed by the Mean Squared Error (MSE), displayed within the figure, which compares the illuminated region to the ground truth.

Second, although both LSQML and BH-GD use gradient descent steps, BH-GD exhibits faster convergence. This is because BH-GD employs a direct formula for calculating a joint step size for all variables (cf. formula (14)), while LSQML calculates the step size approximately and independently for each variable, see [16] for details.

Third, although the Adam method uses a constant gradient step length manually adjusted for

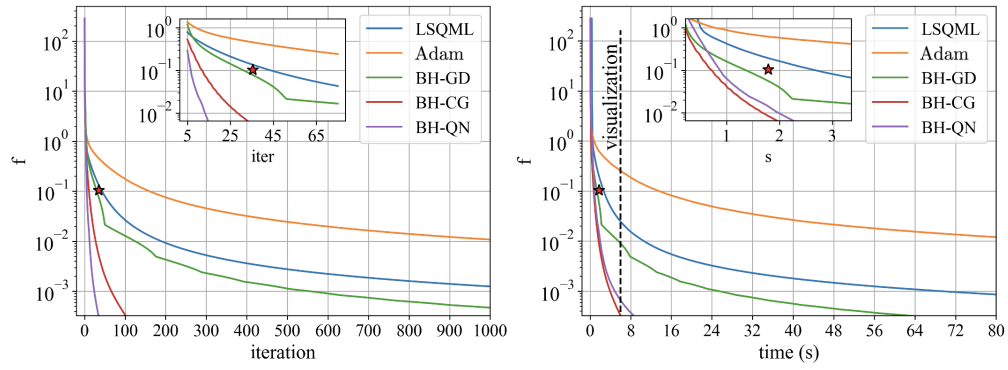


Fig. 3. Objective functional value vs. iteration number (left) and vs. computation time (right) when reconstructing the object and probe from synthetic data.

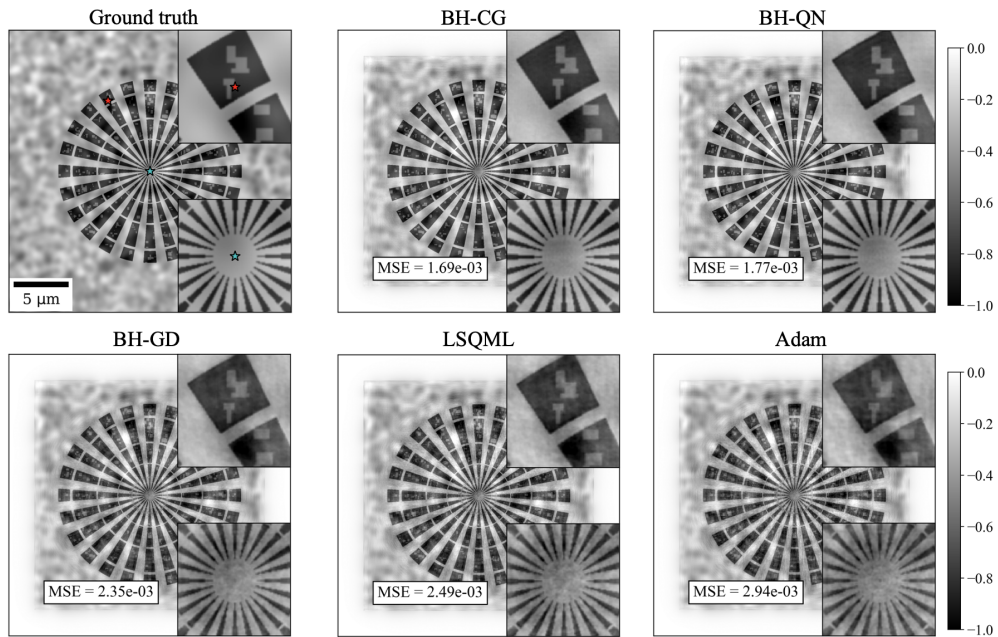


Fig. 4. Reconstruction results (object phase) for a synthetic siemens star after 6 s execution of different methods. Corresponding states of the objective functional are marked with line 'visualization' in Figure 3.

optimal convergence speed, it ultimately performs slower than methods that adjust the step size for each iteration. This is evident when comparing the Adam, LSQML, and BH-GD plots in the left and right panels. This highlights the disadvantage of automatic differentiation methods in achieving faster convergence, particularly in more complex problems.

Finally, it is worth comparing the two leading methods, BH-CG and BH-QN. While BH-QN requires fewer iterations to converge, BH-CG shows slightly faster performance when considering the functional vs. time plot. This is because BH-QN involves solving (19) iteratively. In these tests we solve the problem approximately by gradually increasing the number of inner iterations. Specifically, we set the number of inner iterations to  $\max(5, \lfloor \frac{k}{2} \rfloor)$ , where  $k$  represents the outer iteration in the main optimization problem. Additionally, for stability, we perform the first three outer iterations as standard conjugate gradient iterations. We believe this strategy could be further optimized, for example, by monitoring the residual at each inner iteration and stopping when the residual falls below a certain threshold. We plan to explore these improvements in future work.

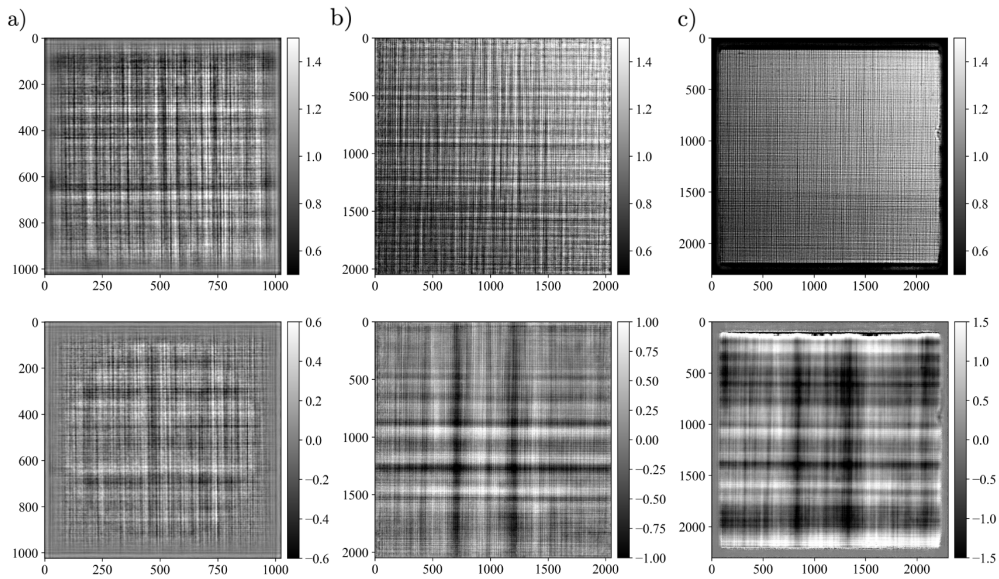


Fig. 5. Probes recovered during reconstruction of a) synthetic data from Figure 2, b) experimental Siemens star data from Figure 6, and c) experimental coded aperture data from Figure 9

## 8.2. Experimental data: object and probe retrieval

As the first experimental dataset, we consider measurements of a 200 nm thick gold Siemens star at beamline ID16A of the ESRF. This object is routinely used at the beamline for optics calibration and resolution tests. Acquisition parameters, along with an example of the acquired data, are shown in Figure 6. The data were measured for 16 object positions chosen based on the strategy described in [1]. Unlike the synthetic tests, where the propagation distance was specified initially, here we begin with the distances defined in cone beam geometry and convert them to parallel beam geometry. This conversion ensures proper rescaling of coordinates based on the Fresnel scaling theorem [30]. Further details on this process can be found in the Appendix of [31].

In this experiment, the linear stages moving the sample laterally were highly precise. Preliminary reconstruction using the BH-CG method with position correction enabled showed that the

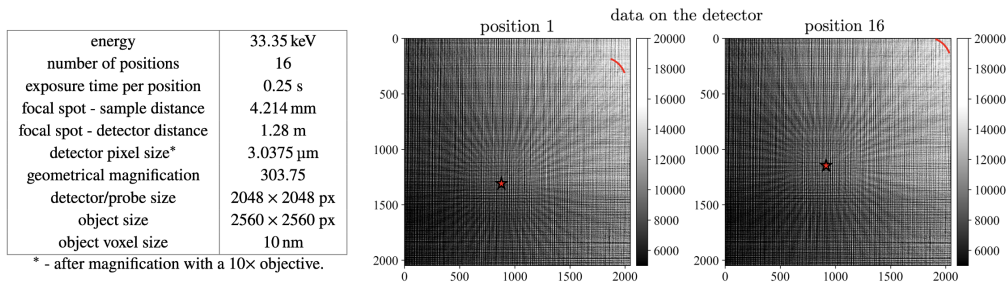


Fig. 6. Data acquisition parameters and examples of measured data for near-field ptychography of the 200 nm thick gold Siemens star at beamline ID16A of ESRF.

positional error was less than 0.15 pixels. Consequently, we performed reconstructions with various methods without position correction, similar to the approach used for the synthetic data in the previous section. Prior to reconstruction, we also applied "zinger removal", a common pre-processing procedure including the median filter to eliminate isolated bright pixels which can result from malfunctioning detector regions or parasitic scattering.

Similar to the synthetic data test, for the initial estimate of the sample transmittance function  $\psi$ , we used the reconstruction obtained from the Paganin method, applied to the data divided by the reference image. For the initial estimate of the probe function  $q$ , we used the square root of the reference image, propagated back to the sample plane.

Convergence plots in Figure 7 again demonstrate that second-order methods significantly outperform the other ones. Now the BH-CG is even more than 10 times faster than BH-GD. LSQML and BH-GD demonstrate similar convergence rate during first 200 iterations, however, iterations with the BH-GD is faster yielding better overall performance. Again, Adam is found to yield very slow convergence.

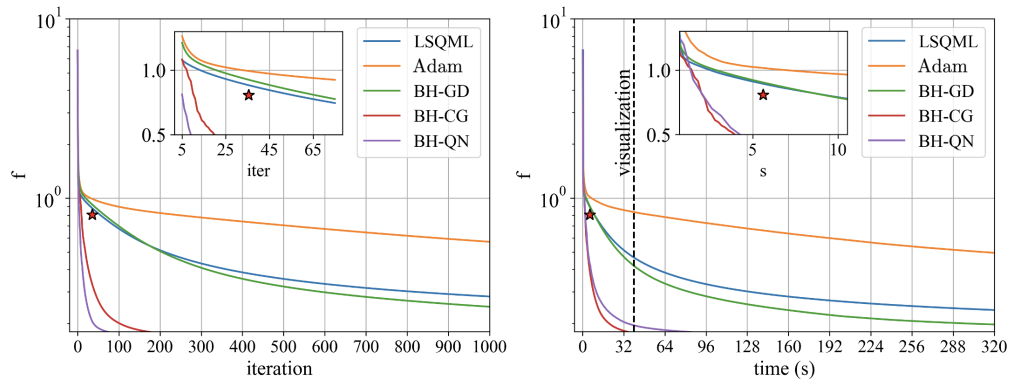


Fig. 7. Objective functional value vs. iteration number (left) and vs. computation time (right) when reconstructing the object and probe from experimental Siemens star data acquired at ID16A of ESRF.

There is a difference in performance of BH-CG and BH-QN for this experimental dataset. While BH-QN converges in fewer iterations, its overall performance appears slower—roughly twice as slow as BH-CG. As seen in the right panel of Figure 7, BH-CG reaches the bottom of the plot at 32 seconds, whereas BH-QN reaches it at 64 seconds.

Figure 8 shows the reconstruction results after executing each method for 40 seconds, with

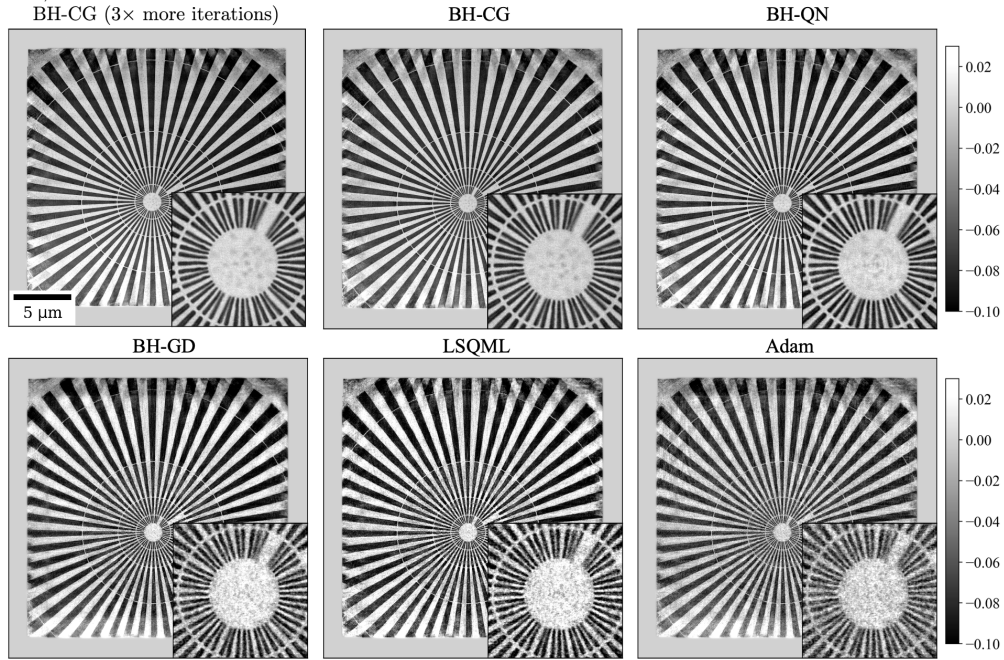


Fig. 8. Reconstruction results for experimental gold Siemens star data from ID16A of ESRF after 40 s execution of different methods and 120 s ( $3\times$  more iteration) of BH-CG for reference. Corresponding states of the objective functional are marked with line 'visualization' in Figure 7.

an additional image showing 120 seconds ( $3\times$  more iterations) of execution for BH-CG as a reference. The reconstructed probe is shown in Figure 5,b. Corresponding states of the objective functional are marked with line 'visualization' in Figure 7.

Both BH-CG and BH-QN produce high-resolution results, with the smallest features of the Siemens star clearly separable and dust particles in the center visible. BH-QN exhibits a noticeable difference in the middle region compared to BH-CG. This difference disappears after 60 s execution of BH-QN. In contrast, the reconstructions from BH-GD, LSQML, and Adam are noisy and far from converged, with small features not visible.

The performance improvement achieved by the proposed approach could be a key consideration for the ptychography community, as it has the potential to significantly accelerate data processing at synchrotron beamlines. Based on our experience, it has been claimed that phase retrieval reconstruction in 3D ptychography (ptychography for different object rotation angles) may take up to one week, but the proposed second-order methods can potentially complete this in less than a day.

### 8.3. Experimental data: object, probe, and position correction

In this section, we demonstrate the simultaneous reconstruction of the object, probe, and position correction, as described in Section 7, using experimental data from a coded aperture sample collected at ID16A of ESRF. The data were acquired as part of a project developing a single-distance holotomography method using coded apertures [32]. The coded aperture used is a binary gold mask with a  $2\ \mu\text{m}$  bin size and  $2\ \mu\text{m}$  thickness. Compared to the 200 nm gold Siemens star sample from the previous section, the coded aperture introduces larger phase shifts in the wavefront, making it more suitable for characterizing the illumination structure, i.e., for

reconstructing the probe.

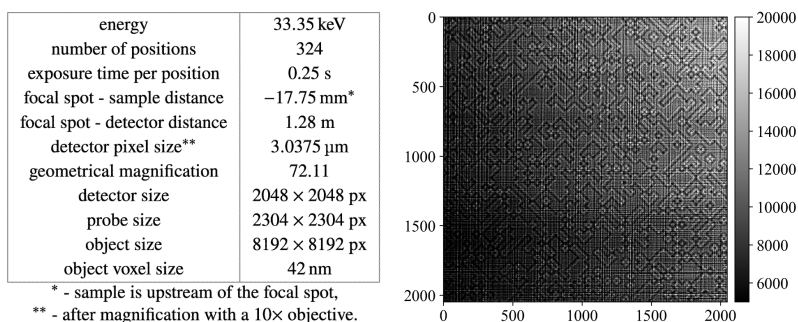


Fig. 9. Data acquisition parameters and an example of measured data for near-field ptychography of the coded aperture at beamline ID16A of ESRF.

The data acquisition settings and an example of the acquired data are shown in Figure 9. Notably, in contrast to the Siemens star experiment, the coded aperture was placed upstream of the focal spot, as this configuration produces better structured illumination compared to placing it downstream. While studying structured illumination is beyond the scope of this work, it is important to note that for the approach with the coded aperture to work, accurate reconstruction of both the probe and the coded aperture is essential. This was achieved using the near-field ptychography method that we study in this work. In this experiment, the coded aperture movement was not controlled by precise motors, so position refinement is necessary.

Before reconstruction we obtained a coarse estimate for the position errors using cross correlation of adjacent diffraction patterns. As with the Siemens star dataset, we applied zinger correction and computed the initial guess for the sample using the Paganin method, while the initial probe estimate was obtained by backpropagating the square root of the reference image.

In contrast to the Siemens star experiment, the probe reconstruction was performed on a grid larger than the detector size since it is possible to reconstruct the probe outside the detector's field of view. The oscillations (fringes) initiated from the regions outside the field of view propagate back into it, allowing us to use this information to reconstruct the areas outside the detector's view. Specifically the probe size is 2304  $\times$  2304, while the detector is 2048  $\times$  2048. Additionally, in this experiment, the object was reconstructed on a significantly larger grid, 8192  $\times$  8192, using 324 positions. Compared to previous cases with only 16 positions, this provides sufficient data for an accurate reconstruction of the probe, even in regions outside the detector's field of view.

For demonstration, we perform the reconstruction using only the BH-CG method and analyze the convergence behavior with and without position correction. We do not compare this method to others, as different implementations of position correction exist across various packages, often functioning as independent supplementary steps rather than being integrated into the object and probe optimization process.

It is important to note that the entire dataset and auxiliary variables in the BH-CG method do not fit into GPU memory. As a result, we implemented data chunking and optimized data transfers between the CPU and GPU for processing. For reference, the reconstruction time for 150 iterations using the BH-CG method was approximately 1.5 hours.

The reconstruction results for the coded aperture sample are shown in Figure 10. The convergence plot in the left part of the figure indicates that with position correction enabled, the BH-CG method minimizes the objective functional to values below  $10^2$  within 150 iterations. In contrast, when position correction is disabled, the functional remains above  $10^3$ . Reconstruction results, shown in the right part of the figure, display the full coded aperture image and zoomed-in regions containing various features. It is clear that position correction significantly enhances

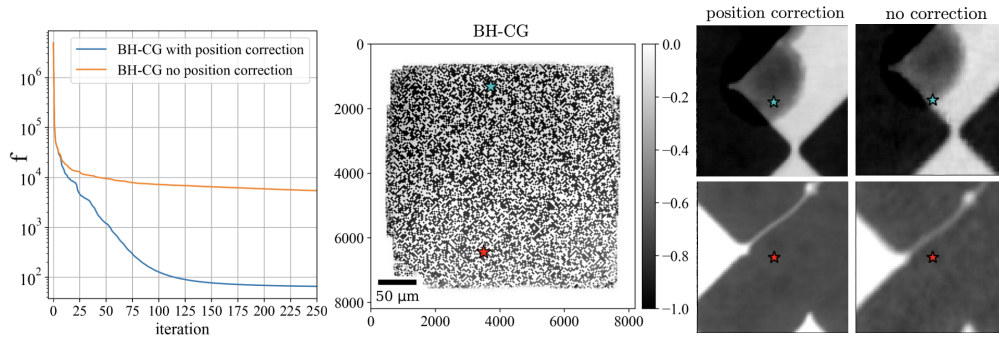


Fig. 10. Objective functional value vs. iteration number when reconstructing the coded aperture object and probe with and without position correction from data acquired at ID16A of ESRF.

image sharpness, thereby improving spatial resolution. The found floating-point position errors in the horizontal and vertical directions are in the range  $(-8, 8)$ , demonstrating the effectiveness of the proposed method compared to the standard cross-correlation approach.

Finally, it is interesting to analyze the reconstructed probe in this experiment, shown in Figure 5,c. The probe is accurately reconstructed even outside the field of view. The slits that limit the beam illumination are clearly visible as black regions on either side of the probe. These slits do not appear in the measured data (right part of Figure 9), yet they are successfully recovered due to the propagation of fringes originating from regions outside the field of view into the reconstructed area.

## 9. Conclusion

In this work, we introduced an innovative ptychography reconstruction method that leverages the bilinear Hessian and Hessian operators to significantly accelerate the convergence of iterative schemes for refining the object, probe, and position parameters. We provided the necessary mathematical formulations to implement gradient descent, conjugate gradient, and quasi-Newton schemes, tailored for both Gaussian and Poisson noise models. As a demonstration of its effectiveness, we applied our method to both synthetic and experimental near-field ptychography data. The proposed second-order methods outperform traditional techniques by one order of magnitude, showcasing their remarkable efficiency in handling large-scale ptychography datasets. This represents a substantial contribution to the field of ptychography, where high-quality reconstructions are typically computationally expensive. While phase retrieval reconstruction in 3D ptychography (which involves capturing data at different object rotation angles) can take up to a week using conventional methods, our proposed techniques can achieve the same result in under a day. This improvement drastically reduces the time required for image reconstruction, which has profound implications for both research and industrial applications, particularly in in-situ ptychography experiments, where immediate feedback is crucial for adjusting environmental conditions and optimizing the sample for better imaging.

Looking ahead, there are several exciting avenues for further research and development. One major goal is to adapt our method for processing experimental far-field ptychography data, which presents distinct challenges compared to near-field data. Key advancements will include multimode probe reconstruction, which can improve the robustness of the method in the presence of complex sample geometries, and orthogonal probe relaxation [33] to minimize artifacts in the reconstructed images. Additionally, we plan to implement batch data processing techniques that can further accelerate the convergence of our iterative schemes [16, 34]. Although



adapting our method for multimode probes and orthogonal relaxation is expected to be relatively straightforward, batch data processing has not been fully explored with conjugate gradient methods and will be a challenging but valuable addition to our toolkit.

In parallel, we are actively exploring the application of our method to 3D ptychography, where the corresponding 2D ptychography and subsequent tomography problems are solved jointly. As demonstrated in previous studies (e.g., [17, 35]), the joint reconstruction not only improves the reconstruction quality but also reduces the number of measurements required, both in terms of scanning positions and rotation angles. This reduction in measurement overhead has the additional benefit of decreasing the radiation dose delivered to sensitive samples, which is critical in fields such as biological imaging and materials science, where sample preservation is paramount.

In addition to tackling these methodological challenges, we recognize the need to develop efficient computational strategies to manage large datasets generated by 3D ptychography. The massive data volumes involved necessitate optimized solutions for distributed computations across multiple GPUs and computing nodes, ensuring that the reconstruction process remains feasible even for the most complex experiments. Moreover, improving memory efficiency and parallelization will be key to making our approach scalable for even larger datasets.

## Acknowledgments

This research used resources of the Advanced Photon Source, a U.S. Department of Energy (DOE) Office of Science user facility and is based on work supported by Laboratory Directed Research and Development (LDRD) funding from Argonne National Laboratory, provided by the Director, Office of Science, of the U.S. DOE under Contract No. DE-AC02-06CH11357. We acknowledge the European Synchrotron Radiation Facility (ESRF) for provision of synchrotron radiation facilities under proposal number MI-1506 and we would like to thank Peter Cloetens for assistance and support in using beamline ID16A.

## Disclosures

The authors declare no conflicts of interest.

## Data availability

Data underlying the results presented in this paper are not publicly available at this time but may be obtained from the authors upon reasonable request.

## References

1. M. Stockmar, P. Cloetens, I. Zanette, *et al.*, “Near-field ptychography: phase retrieval for inline holography using a structured illumination,” *Sci. reports* **3**, 1927 (2013).
2. R. M. Clare, M. Stockmar, M. Dierolf, *et al.*, “Characterization of near-field ptychography,” *Opt. express* **23**, 19728–19742 (2015).
3. J. Rodenburg, “Ptychography and related diffractive imaging methods,” *Adv. Imag. Elec. Phys.* **150**, 87–184 (2008).
4. J. Rodenburg and A. Maiden, “Ptychography,” *Springer Handb. Microsc.* pp. 819–904 (2019).
5. M. Holler, M. Guizar-Sicairos, E. H. Tsai, *et al.*, “High-resolution non-destructive three-dimensional imaging of integrated circuits,” *Nature* **543**, 402–406 (2017).
6. S. H. Shahmoradian, E. H. Tsai, A. Diaz, *et al.*, “Three-dimensional imaging of biological tissue by cryo x-ray ptychography,” *Sci. reports* **7**, 6291 (2017).
7. F. Monaco, M. Hubert, J. C. Da Silva, *et al.*, “A comparison between holographic and near-field ptychographic x-ray tomography for solid oxide cell materials,” *Mater. Charact.* **187**, 111834 (2022).
8. T. Aidukas, N. W. Phillips, A. Diaz, *et al.*, “High-performance 4-nm-resolution x-ray tomography using burst ptychography,” *Nature* **632**, 81–88 (2024).
9. J. Qian, C. Yang, A. Schirotzek, *et al.*, “Efficient algorithms for ptychographic phase retrieval,” *Inverse Probl. Appl. Contemp. Math* **615**, 261–280 (2014).

10. H. Chang, L. Yang, and S. Marchesini, "Fast iterative algorithms for blind phase retrieval: A survey," in *Handbook of Mathematical Models and Algorithms in Computer Vision and Imaging: Mathematical Imaging and Vision*, (Springer, 2023), pp. 139–174.
11. L.-H. Yeh, J. Dong, J. Zhong, *et al.*, "Experimental robustness of fourier ptychography phase retrieval algorithms," *Opt. express* **23**, 33214–33240 (2015).
12. J. W. Daniel, "The conjugate gradient method for linear and nonlinear operator equations," *SIAM J. on Numer. Anal.* **4**, 10–26 (1967).
13. W. W. Hager and H. Zhang, "A survey of nonlinear conjugate gradient methods," *Pac. journal Optim.* **2**, 35–58 (2006).
14. N. Andrei *et al.*, *Nonlinear conjugate gradient methods for unconstrained optimization* (Springer, New York, 2020).
15. M. Carlsson, V. Nikitin, E. Troedsson, and H. Wendt, "The bilinear hessian for efficient large scale optimization," *arXiv:2502.03070* (2025).
16. M. Odstrčil, A. Menzel, and M. Guizar-Sicairos, "Iterative least-squares solver for generalized maximum-likelihood ptychography," *Opt. express* **26**, 3108–3123 (2018).
17. V. Nikitin, S. Aslan, Y. Yao, *et al.*, "Photon-limited ptychography of 3d objects via bayesian reconstruction," *OSA Continuum* **2**, 2948–2968 (2019).
18. A. S. Jurling and J. R. Fienup, "Applications of algorithmic differentiation to phase retrieval algorithms," *JOSA A* **31**, 1348–1359 (2014).
19. S. Kandel, S. Maddali, M. Allain, *et al.*, "Using automatic differentiation as a general framework for ptychographic reconstruction," *Opt. express* **27**, 18653–18672 (2019).
20. F. Srajer, Z. Kukulova, and A. Fitzgibbon, "A benchmark of selected algorithmic differentiation tools on some problems in computer vision and machine learning," *Optim. Methods Softw.* **33**, 889–906 (2018).
21. S. Kandel, S. Maddali, Y. S. Nashed, *et al.*, "Efficient ptychographic phase retrieval via a matrix-free levenberg-marquardt algorithm," *Opt. Express* **29**, 23019–23055 (2021).
22. M. R. Hestenes, E. Stiefel *et al.*, *Methods of conjugate gradients for solving linear systems*, vol. 49 (NBS Washington, DC, Washington, 1952).
23. R. Fletcher and C. M. Reeves, "Function minimization by conjugate gradients," *The computer journal* **7**, 149–154 (1964).
24. E. Polak and G. Ribiere, "Note sur la convergence de méthodes de directions conjuguées," *Revue française d'informatique et de recherche opérationnelle. Ser. rouge* **3**, 35–43 (1969).
25. Y.-H. Dai and Y. Yuan, "A nonlinear conjugate gradient method with a strong global convergence property," *SIAM J. on optimization* **10**, 177–182 (1999).
26. W. W. Hager and H. Zhang, "A new conjugate gradient method with guaranteed descent and an efficient line search," *SIAM J. on optimization* **16**, 170–192 (2005).
27. A. M. Maiden and J. M. Rodenburg, "An improved ptychographical phase retrieval algorithm for diffractive imaging," *Ultramicroscopy* **109**, 1256–1262 (2009).
28. P. Thibault, M. Dierolf, A. Menzel, *et al.*, "High-resolution scanning x-ray diffraction microscopy," *Science* **321**, 379–382 (2008).
29. T. E. Gureyev and K. A. Nugent, "Phase retrieval with the transport-of-intensity equation. ii. orthogonal series solution for nonuniform illumination," *JOSA A* **13**, 1670–1682 (1996).
30. D. Paganin, *Coherent X-ray optics*, 6 (Oxford University Press, USA, 2006).
31. V. Nikitin, M. Carlsson, D. Gürsoy, *et al.*, "X-ray nano-holotomography reconstruction with simultaneous probe retrieval," *Opt. Express* **32**, 41905–41924 (2024).
32. V. Nikitin, M. Carlsson, R. Mokso, *et al.*, "Single-distance nano-holotomography with coded apertures," *Opt. Lett.* **50**, 574–577 (2025).
33. M. Odstrčil, P. Baksh, S. Boden, *et al.*, "Ptychographic coherent diffractive imaging with orthogonal probe relaxation," *Opt. express* **24**, 8360–8369 (2016).
34. A. Tripathi, Z. Wendy Di, Z. Jiang, and S. M. Wild, "Stochastic minibatch approach to the ptychographic iterative engine," *Opt. Express* **32**, 30199–30225 (2024).
35. S. Aslan, V. Nikitin, D. J. Ching, *et al.*, "Joint ptycho-tomography reconstruction through alternating direction method of multipliers," *Opt. Express* **27**, 9128–9143 (2019).